Cadmium Sulfide Embedded Prussian Blue as Highly Active Bifunctional Electrocatalyst for Water-Splitting Process

By

Uzair Abdullah

School of Chemical and Materials Engineering

National University of Sciences and Technology

2022

Cadmium Sulfide Embedded Prussian Blue as Highly Active Bifunctional Electrocatalyst for Water-Splitting Process

Name: Uzair Abdullah

Reg.No:00000320350

This thesis is submitted as a partial fulfillment of the requirements for the degree of

‘’MS in Chemical Engineering’’

Supervisor Name: Dr. Erum Pervaiz

School of Chemical and Materials Engineering (SCME)

National University of Sciences and Technology (NUST)

H-12 Islamabad, Pakistan

March 2022

Dedication

By the mercy of Almighty Allah, the Most Merciful and Most Beneficent, this study is dedicated to my parents, who have always provided me with direction and support. To my supervisor, who shared her knowledge, provided me guidance, and pushed me to complete my objectives. And to all my coworkers with whom I've enjoyed wonderful memories.

Acknowledgement

There is none other but Almighty Allah, whose will be required for everything and anything in this world, who blessed us with the ability to think and made us willing to explore the entire universe. Infinite greetings to the Holy Prophet Muhammad (PBUH), the cause of the universe's creation and a fountain of knowledge and blessing for all of humanity.

Dr. Erum Pervaiz, my renowned supervisor, deserves credit for trusting in my talents. His constant guidance, encouragement, and support were vital in the project's success. I'd want to express my heartfelt gratitude to my deserving GEC members, Dr. Sara Farrukh, and Dr. Tayyaba Noor. I've never given it much thought. Having said that, the unwavering moral support that my family and friends have always provided will always be my light in the dark. My heartfelt gratitude goes out to all the personnel and lab attendants Thank you!

Abstract

Process of water-splitting to produce hydrogen has limited application at commercial-scale. As substantial overpotential is required at anode for the Oxygen Evolution Reaction (OER) and at cathode for the Hydrogen Evolution Reaction (HER). CdS as semiconductor possess remarkable chemical stability for redox reactions, high absorption capacity, diverse morphologies, and negative conduction band edge. Photo and electrocatalytic applications of CdS and its hybrids include low cost and green water-splitting for H_2 generation. We present an interface engineering strategy for constructing an effective bifunctional electrode material for the water splitting process by using CdS-NRs@PBNPs heterostructures.

These bifunctional electrocatalyst have demonstrated improved water splitting performance, for both HER and OER processes. For HER, the optimized hybrid CdS-NRs@PBNPs (1:1) shows significantly improved catalytic performance with low overpotentials of 126 mV and 181 mV, respectively, at current densities of 10 $mA.cm^{-2}$ and 20 $mA.cm^{-2}$. Similarly, for OER it displays an overpotential of 250 mV and 316 mV at current densities of 10 $mA.cm^{-2}$ and 20 $mA.cm^{-2}$. Furthermore, the CdS-NRs@PBNPs(1:1) has demonstrated long-standing stability of 20 hours. The hybrid's enhanced OER and HER activity is attributable to a synergetic impact between CdS-NRs and PBNPs, as well as the active site modification due to the presence of Cadmium and iron in the hybrid.

Key Words: Electrochemical Water splitting, Cadmium sulfide, Prussian Blue Hydrogen Evolution Reaction (HER), Oxygen Evolution Reaction (OER)

Table of Contents

List of figures

List of Tables

Abbreviations

CdS-NRs: Cadmium Sulfide Nano Rods

PBNPs: Prussian Blue Nano Particles

MOF: Metallic Organic framework

FE: Faradaic Efficiency

Oxidation: Ox

Reduction: Red

dec^{-1}: Deca

Chapter 1

1. Introduction

Significant increase in global energy demand leads to increased exploitation of fossil fuels resulting in global warming and other environmental concerns along with continuous increase in energy reserves. To combat environmental pollution and to support future energy requirements; mankind is prompted to seek renewable energy sources for a sustainable future. Researchers are trying to develop pollution-free processes for surrogate energy reservoirs and environment decontamination with the aim to associate human civilization growth with sustainability[1]. The high energy density, clean, and renewable nature of hydrogen fuel has attracted a lot of interest as the fuel of the future [2, 3]. Several processes and strategies are being developed for commercial scale economical green resources and environmental cleansing. These processes include high energy density of H_2 fuel production, purification and treatment of contaminated water and conversion of CO_2 to fuels etc. [4, 5]. Eco-friendly processes according to the current studies are very efficient with low or no carbon footprints but are very expensive and energy-intensive as well [6].

To date, Hydrocarbon cracking, methane reforming and other techniques are being used to generate hydrogen gas as a fuel at commercial scale. However, these processes are very harmful to the environment and contribute to the greenhouse effect. Water-splitting is a green alternative to the traditional hydrogen production processes as it produces pure hydrogen with almost negligible carbon emissions. However, it is tedious and energy-intensive to break the hydrogen bond between the O_2 and H_2 of water. The process requires a catalyst to operate in a favorable manner [7-10]. A suitable catalyst can boost up the process, so all the constraints are fully utilized to make cost-conscious.

Cadmium Sulfide is a semiconductor material with a narrow band gap of around 2.4 eV, low cost, large number of polymorphs and excellent optical/electronic properties [11] making it an extensively studied material for solar energy utilization [12]. These inherent characteristics make CdS suitable for photocatalytic and electrocatalytic water

splitting, photocatalytic CO_2 reduction, photocatalytic organic pollutants degradation etc. [13-15]. Due to some excellent featuring properties of CdS based hybrids with different materials reported because of its distinctive properties and chemistry [16, 17]. CdS has excellent charge carrier transportation capability, which restrict the recoupling of photogenerated electron-hole pairs and makes it feasible to be transferred from one point to other in an efficient way which eventually leads to enhanced photocatalytic/electrocatalytic performance. The subject of research is to develop easily fabricated, cost-effective, durable, non-polluting, and abundantly available catalyst for the process. For this, a variety of innovative materials, such as CdS, TiO_2, ZnS, and ZnO etc. have been explored [18]. CdS (a typical II-VI n-type semiconductor) is being actively researched as a typical anode material for water splitting on account of its simple synthesis and appropriate band gap of 2.4 eV [19]. Additionally, CdS has a conduction band which is less negative compared to the reduction potential of H^+/H_2. Several nanomaterial morphology including nanorods [20], quantum dots [21], nanowires [22], nanoflowers [23], and nanosheets [24] have been used as electrodes in electrochemical cells for water splitting. CdS is slightly unstable and have poor charge separation properties. To date, several methodologies have been used to increase the electrochemical semiconductors based catalyst, including doping with elements [25], modification with precious metallic nanoparticles [26] and heterostructure formation [27].

A lot of research on MOF and semiconductor heterojunctions were published, with cadmium sulfide (CdS) receiving special interest as an efficient semiconductor materials because of its light-harvesting capabilities and size-dependent electrical and optical characteristics [28, 29]. Several studies show that transition metal based electrocatalysts mostly serve as co-catalysts to improve charge transportation/separation and offer active surface area for hydrogen production [30, 31]. Water reduction and oxidation is an important interfacial reaction process that happens primarily on the surface of catalysts. It is acknowledged that MOFs based catalysts with unique morphology, numerous active sites, and large volume are excellent methods for increasing the capability of electrocatalysts [32]. Moreover, bimetallic MOFs-derived electrocatalysts for water electrolysis are extensively studied. Despite significant efforts

to enhance the electrocatalytic behavior of MOFs-derived bimetallic catalyst, the effectiveness of the catalytic and electrolytic processes remains incompatible with conventional noble metal catalysts [33].

Prussian blue (a subtype of MOF) has emerged as a novel framework for synthesis of various composites. For efficient transfer the electron-hole pairs, soluble PB and alkali metal cations exchange water molecules in their cavities. Using cyano-bridged ligands, PB is built into Nano-sized frameworks: PBNPs. Stability, solubility, porosity, flexible molecular structure, low density, and changeable physical and chemical characteristics are some of the interesting aspects of these PB complexes [34]. Electrocatalysts, Electrochromic displays, secondary batteries, hydrogen storage, and ion- and biosensors are few of the many scientific and industrial applications of PB [35].

In this study, CdS nano rods were successfully constructed by solvothermal method. We described a self-assembly approach for making CdS-NRs based PBNPs precursors and a one-step sonication procedure for manufacturing CdS-NRs@PBNPs composites with improved electrochemical activity against OER and HER. This improved activity can be ascribed to its structure, increased available specific area, synergetic influence of the bi-metal presence, fast charge and mass transfer ability. These properties are responsible for promoting the contact of reactant to the active sites.

1.1 Fundamentals of Water Splitting Process

An electrochemical water splitting cell consists of an anode, cathode, aqueous electrolyte and an external bias [36, 37]. The overall water splitting mechanism is combination of two half reactions OER and HER that take place at the cathode and anode, respectively. Figure 1 depicts the basic components of an overall water splitting system. Pure H_2 and O_2 gases are generated from the cathode surface and anode surface, respectively, during the electrolytic water splitting process. Mechanism followed depends on the electrolyte being used.

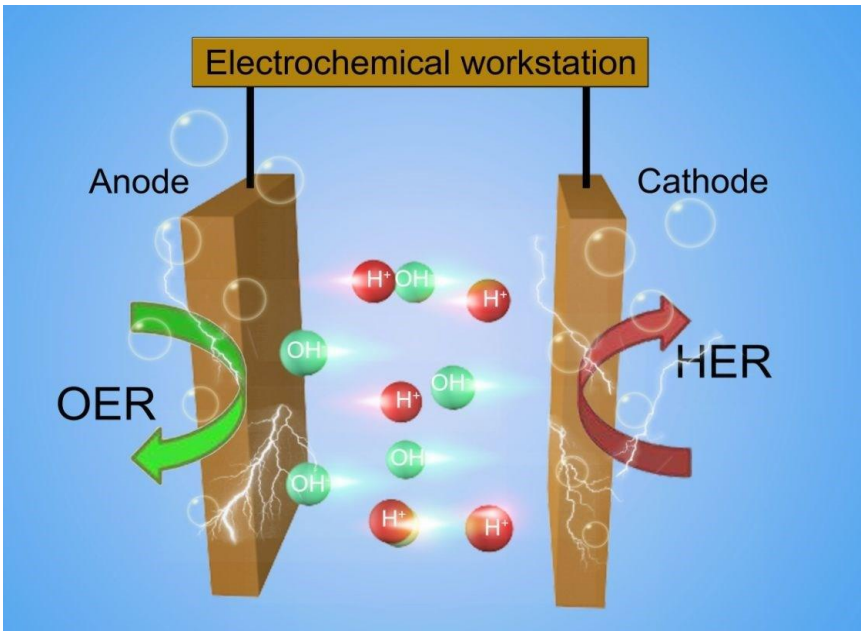

Figure 1: Represents the overall water splitting process (OER at anode to produced O_2 and HER at cathode produced H_2 Via reduction of H^+). Exclusive copy rights 2021 Li, W., et al. [38]

In an acidic electrolyte

For HER $4H^+ + 4e^- \longrightarrow 2H_2$ E=0V Eq.1

For OER $2H_2O + 4e^- \longrightarrow O_2 + 4H^+$ E=1.23V Eq.2

In basic electrolyte

For HER $4H_2O + 4e^- \longrightarrow 2H_2 + 4OH^{-1}$ E=0.828V Eq.3

For OER $4OH^{-1} - 4e^- \longrightarrow 2H_2O + O_2$ E=0.402V Eq.4

Overall water splitting reaction

$$2\,H_2O \longrightarrow 2\,H_2 + O_2 \qquad \text{Eq.5}$$

At 1 atm and 298 K, the potential thermodynamical voltage required for water splitting is 1.23 V, irrespective of whether the electrolyte is alkaline or acidic in nature [39]. However, the electrolyzing water operation voltage is slightly greater than 1.23 V. Due to intrinsic activation impediment, the surplus potential is described as overpotential.

$$E_{OP} = E + E_A + E_C + E_R \qquad E=1.23\ V \qquad \text{Eq.6}$$

From above equation E_A is the anode overpotential for OER, E_C is the cathode overpotential for HER, E_R and indicates the excessive potential generated by electrolytic diffusion, surface polarization, and further counter electro-motive force

sources. Between these considerations, E_C and E_A are essential for electrocatalyst operation at the cathode and anode surface against OER and HER, respectively. As a result, by using the electrocatalysts as cathode and anode materials, E_A and E_C can be greatly reduced, and the electrocatalytic behavior of water splitting can be improved to gain a large yield [38].

1.1.1 Hydrogen Evolution Reaction (HER)

Hydrogen evolution reaction is two electrons transfer mechanism that occurs on the cathode in two stages. In the meantime, during the electrochemical reaction, these two stages entail two common pathways known as the Volmer-Tafel and Volmer-Heyrovsky processes as shown in Figure 2.

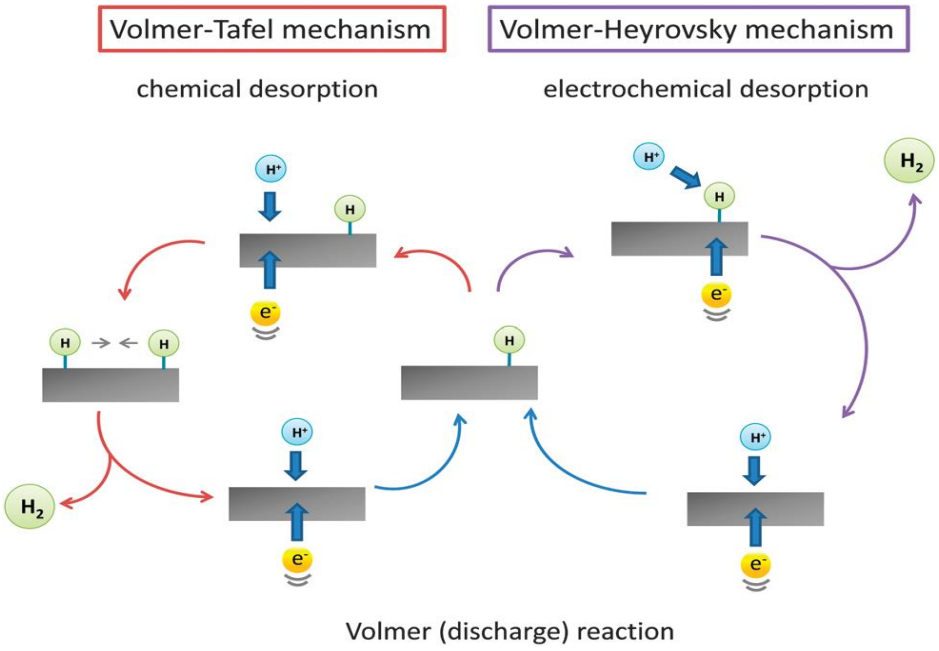

Figure 2 In acidic solutions, the H_2 evolution mechanism on the surface of an electrode. Exclusive copy rights 2014 Morales, C.G., et.al.[40].

The Volmer-Tafel and Volmer-Heyrovsky mechanisms follows desorption phenomena both chemical and electrochemical, respectively. The reactions mentioned below

Volmer reaction

The Volmer reaction is a process in which hydrogen adsorption occurs by the electrochemical method. In the acidic solution the proton reacts with the electron on the catalytic surface to produce the active intermediate H*.

In acidic solution

$$H^+ + M + e^- \longrightarrow M\text{-}H^* \quad \text{Eq.7}$$

In alkaline solution

$$H_2O + M + e^- \longrightarrow M\text{-}H^* + OH^- \quad \text{Eq.8}$$

Heyrovsky reaction

The Heyrovsky reaction is a type of electrochemical desorption process. In an acidic electrolyte, H* interacts with H^* and electrons to form H_2 molecules.

In acidic solution

$$M\text{-}H^* + H^+ + e^- \longrightarrow M + H_2 \quad \text{Eq.9}$$

Tafel reaction

The chemical desorption mechanism occurs as two adsorbed H* molecules on the catalytic surface combine to produce H_2.

In acidic or alkaline solution

$$2M\text{-}H^* \longrightarrow 2M + H_2 \quad \text{Eq.10}$$

1.1.2 Oxygen Evolution Reaction

In comparison to HER at the cathode, at the anode the OER is a 4-electron transfer mechanism through several intermediates. Because of the multistep mechanism and high energy requirement, the OER is kinetically sluggish with a high overpotential compared to the hydrogen evolution reaction (HER). Moreover, OER is strongly dependent on the value of pH of the electrolytic nature solution since it operates differently in acidic and basic media. The oxidation process of two H_2O molecules in acidic and neutral media produces hydrogen and oxygen by using 0.404V potential. In this alkaline medium, the OH^- group is converted into O_2 and H_2O by utilizing 1.230 V (vs RHE). It can be concluded from the preceding that the mechanism operates less efficiently in an acidic atmosphere than in an alkaline environment [41, 42].

Following reactions takes place during OER:

In Acidic Electrolyte

$$H_2O + M \longrightarrow M\text{-}^*OH + H^+ + e^- \quad \text{Eq.11}$$

$$M\text{-}^*OH \longrightarrow M\text{-}O^* + H^+ + e^- \quad \text{Eq.12}$$

$$M\text{-}O^* + H_2O \longrightarrow M\text{-}^*OOH + H^+ + e^- \quad \text{Eq.13}$$

$$M\text{-}^*OOH \longrightarrow M + O_2 + H_2O + e^- \quad \text{Eq.14}$$

In Alkaline Electrolyte

$$OH^- + M \longrightarrow M\text{-}^*OH + e^- \quad \text{Eq.15}$$

$$M\text{-}^*OH + OH^- \longrightarrow M\text{-}O^* + H_2O + e^- \quad \text{Eq.16}$$

$$M\text{-}O^* + OH^- \longrightarrow M\text{-}^*OOH + e^- \quad \text{Eq.17}$$

$$M\text{-}^*OOH + OH^- \longrightarrow M + O_2 + H_2O + e^- \quad \text{Eq.18}$$

It has been reported that several intermediates, such as $^*OH$, O^*, and *OOH, would be generated during the entire OER phase [43]. Furthermore, the electronic structure of an electrocatalyst influences its capability to generate *OOH and adsorb *OH, that has a significant effect on OER efficiency [44].

1.2 Factors Affecting the Overall Water Splitting Process

1.2.1 Band gap

The spectrum responsiveness of the photoconductor is increased when the band gap is reduced. If the band gap is too broad, only a minimal number of necessary intensities of light are absorbed, so the band gap must be narrow enough to accommodate the significant percentage. For PEC water splitting band gap range between 1.6-2.2 enough for absorption of wide band of solar light absorption[45]. The capability of catalysts to transfer charge is critical for achieving effective activity, and it can be enhanced by coupling it with functional materials to increase the charge transfer ability of the catalysts [46].

1.2.2 Crystallinity

In general, studies have shown that as crystallinity increases, catalyst activity increases. This is because high crystallinity inhibits grain boundary development and lattice defects, eliminating electron-hole pair recombination and improving electron transport [47].

1.2.3 Particle Size

Particle size is important factor that affect the catalytic behavior, with a general trend toward small particle size that provide a large specific surface area. The smaller the molecule. Moreover, larger surface area the higher amount of reactant adsorption occurs. It is found that photo catalytic activity does not increase in a logical way as

particle size decreases. Due to the near proximity of the charges, the probability of electron-hole recombination increases as particle size decreases. Therefore, an ideal particle size must be determined [47, 48].

1.3 Evolution Parameters for Overall Water Splitting

Evolution methodologies for the OER, HER, and total water splitting efficiency are required to compare various types of electro catalysts. In overall, the most efficient and scalable approaches for estimating the effectiveness of splitting are the (i) activity, (ii) selectivity, and (iii) stability methods.[49].

1.3.1 Activity

To evaluate the performance of a water-splitting catalyst, many evolution parameters can be employed. For the oxygen evolution process and HER systems, the three most important parameters to evaluate kinetic activity are Tafel slope, current rate, and turnover frequency (TOF). The Tafel slop is a critical characteristic in defining a catalyst's behavior. It's a graph that depicts the relationship between the current generated by an electrochemical cell and the electrode potential of a certain material. It illustrates how the response rate and the overpotential are related. Because a lesser overpotential is required to achieve a high current when the Tafel slope is small, a lesser overpotential is required. [50]. In other words, a catalyst with higher current density and a lower Tafel slope shows greater electrocatalytic activity. The overpotential to attain a current density to 10 mA/cm^2 or higher is widely recognized as an important factor in thermodynamic evolution[51]. The electrode properties have a major effect on the activation overpotential. As a result, selecting the correct catalyst with strong electrocatalytic activity reduces activation overpotential significantly. The TOF reveals how many moles of H2 or O2 are created each unit active center in each amount of time, reflecting the catalyst's intrinsic activity[52-54].

TOF equation represent as

$$TOF = j_A/\alpha f n \qquad \text{Eq.19}$$

j= Current density corresponding to fixed overpotential

A= Electrode area of surface

α= number of transferred electrons

f= Faraday constant

n= The number of moles of contributed materials loaded on surface of electrode.

The effect of both mass and heat transfer, as well as human error, can be avoided with TOF, resulting in reasonably reliable rate calculation.

1.3.2 Selectivity

Selectivity is another important parameter for evaluating electrochemical efficiency in water splitting, but it is seldom considered. The Faradic efficiency technique is used to predict full water decomposition. It is the charge consumed by reactants as a percentage of total charge in an external circuit[55]. Faradaic efficiency is a technique for calculating an OER or HER catalyst's selectivity. Faradaic efficiency, which represents the electron transfer of the catalyst [53].The Faradaic efficiency for the water splitting mechanism can be determined using gas chromatography (GC). The FE value for many previously recorded HER catalysts are 100% using this route. The FE of an OER catalyst, is generally less than 100% due to energy loss from a variety of situations, including heat loss during the electrocatalytic phase, multiple undesired side reactions, and further redox peaks occurring in the potential window of OER.

For OER calculation, the equations are typically used to determine the Faradaic efficiency:

$$\text{Faradaic efficiency} = I_R N_D / I_D N_R N_{CL} \quad \text{Eq.20}$$

I_R=Current at ring

N_D=number of electrons transferred at disc

I_D = Current at disc

N_R= number of electrons transferred at ring

N_{CL}= Collection efficiency of rotating ring disk electrode which is calculated by the response of ferric/ferrous redox system.

When the FE value exceeds 90%, it is typically considered beneficial.

1.3.3 Stability

Catalyst stability will generally be assessed using one of two methods[39, 56]. One is chronoamperometry and second is cyclic voltammetry or LSV measurement are two different types of measurements. The first is to use a fixed potential or current density to observe the variance pattern of current or potential over time. The period of more than ten hours suggests desirable long-term stability. Subsequently a certain number of cycles, the overpotential from LSV curves will generally rise, and a smaller increment of overpotential indicates improved stability.

Chapter 2

Literature Review

2.1 Cadmium Sulfide and their hybrids in photocatalytic water splitting.

CdS and its hybrid are being effectively employed in photocatalytic water-splitting to produce clean H_2 fuel [57]. Other metal sulfide also investigated for water splitting but cadmium sulfide shows best results due to its very suitable conduction and valance band position [16]. However, using pure CdS have certain drawbacks such as photo corrosion, electron-hole pair's recombination, and less surface activity for catalytic reaction. To overcome these problems, CdS are modified [58]. In another effort Xie et al. provides a unique technique for developing ultrathin 2D nano-sheets for nanolayered martials as they synthesized cadmium sulfide nano sheets with thickness of 1nm. It had better photocatalytic activity and was more stable over time. The ultrathin shape and unsaturated surface of S- anions are responsible for the high activity. The driving factor for HER is increased when electrical conductivity improves and recombination of electron-hole pairs decreases due to remarkable structural upshift in the valence and conduction bands. The results show that with the decrease in thickness, increase in H_2 production rate of nanosheets is observed. The average H_2 production rate of 29 mmol/g.hr. respectively under irradiation of visible lights (>420nm) [59].

Jin et al. studied Zn-CdS nano-flowers catalysts and discovered the Crystallinity improves as the quantity of thioacetamide (a source of S) is increased. The recombination of charges decreases when Zn-CdS nanorods self-assemble into nanoflowers. Under visible light irradiation, the greatest photocatalytic activity for H_2 production at a rate of 11,470 mole/g.hr.[60]. Zhang et al. synthesized atomically distributed Ni doped CdS nanorods (NRs) heterostructure photocatalyst with Ni inserting up to 2.8 wt.%. It is the most rebuts catalyst for H_2 evolution at rate of 630 mmol $g^{-1}h^{-1}$. Under optimal conditions, Ni modified CdS nanorods are considered robust photocatalytic HER catalyst. Moreover, the Ni/CdS catalyst exhibited enhanced durability and stability for HER and tremendous photocatalytic performance under

visible light and aerobic environments, representing the great practical value of current reaction system [61] . Honda et al. produced a biological photocatalyst CdS/E.coli hybrid capable of visible range energy transfer and H2 generation in an individual cells in recent study. The recombinant E. coli bacteria were added to CdS precipitation in stages. Under 4-hr light irradiation and pH:7, the H2 generation of 0.05g CdS/ E.coli photocatalyst was 2.7810-8mol[62].

In a study, CdS was synthesized using hydrothermal method, with subsequent loading rate of nickel phosphide nanoparticles on CdS through photochemical reduction method to form two-dimensional hybrid structure. Loading amounts might be modified by photo-deposition time. The CdS/NiP_x exhibited enhanced photocatalytic efficiency than pure CdS. The Optimum H_2 generation rate of 28 mmol /g.hr. with a photo deposition time of 20 minute was observed. The results show that with increase in photo deposition time from 5 minutes to 20 minutes, the H_2 generation rates similarly increased. The CdS-20NiP_x deliver outstanding results with H_2 evolution almost 3.9 fold more than pure CdS can effectively enhance the separation of charges [63]. A ternary CdS/Ag/TiO_2 photocatalyst fabricated for photochemical applications. With the addition of doped materials, good propertied and economical structures were obtained. TiO_2 has high catalytic activity and stability with band gap of 3.2 eV, it is combined with CdS with band gap of 2.4 eV for larger spectra absorption. The photo catalytic activity is further enhanced by incorporation of silver nanoparticles. The fabricated CdS/Ag/TiO_2 composite exhibited enhanced photocatalytic H_2 making rate of 2 mmol $h^{-1}g^{-1}$, which is 1.51 and 2.4 times more than CdS/TiO_2 and pure CdS respectively [64].

Table 1. Photocatalytic Water-Splitting Performance of CdS/TiO_2-based hybrids

Photocatalysts	Synthesis method	Light source	Surface area	Amount of catalyst loading	Sacrificial reagent	Production rate of H_2/ current density	Ref.
CdS NPs/TiO_2 NPs	One-pot combustion Technique	visible light (800-900 Wm^{-2}) 300 W Xe lamp λ≥420 nm	152 m^2g^{-1}	100mg	1M Na_2S + 1M Na_2SO3[65]	11.8 mmol $h^{-1}g^{-1}$	[66]
CdS NPs/ Porous TiO_2 monolith	Hydrothermal and Template sol-gel methods	300 W Xe lamp	65.96 m^2g^{-1}	50mg	0.25M Na_2SO_3 +0.35M Na_2S	1048.7 µmole $h^{-1}g^{-1}$	[67]
CdS Nanowires/TiO_2 Ultrathin layer	Hydrothermal	150 W Xe lamp	1.0 × 1.0 cm^2	_	0.5M Na_2SO_3 + 0.5 M Na_2S	47.5 mmol $h^{-1}g^{-1}$	[67]
g-C_3N_4 Nanosheets/TiO_2-CdS QDs	Hydrothermal	4 LED lamps (3 W, 420 nm)	73.2 m^2g^{-1}	50 mg	0.5M Na_2S + 0.5M Na_2SO_3	1504 µmole $h^{-1}g^{-1}$	[68]
$Ti_3C_2(TiO)_2$ NPs@CdS NPs/MoS_2 NPs	Hydrothermal	300 W Xe lamp, λ > 420 nm	_	10 mg	0.5M Na2SO4	8.47 mmol $h^{-1}g^{-1}$	[69]
CdS nanowire/Ag NPs/ TiO_2 NPs	Hydrothermal	300 W Xe lamp	_	100 mg	10 mL of TEOA + 5 mg of $(NH4)_2$ PtCl6 in 90 mL DI water.	1.91 mmol $h^{-1}g^{-1}$	[64]
TiO_2-Au-CdS	CBD	Visible light (λ ≥ 420 nm, 158 mW/cm 2)	28 m2 g−1	0.1 g	0.1M Na_2S + 0.1M Na_2SO_3	3.50 mmol $h^{-1}g^{-1}$	[70]
Core-shell CdS@TiO_2/Ni_2P	Template CBD	Xe lamp with AM1.5G filter	46.5 m2 g−1	10 mg	0.1M Na_2S + 0.1M Na_2SO_3	13.912 mmol $h^{-1}g^{-1}$	[71]
CdS Nanoflower/TiO_2 nanotube arrays	Hydrothermal	Solar simulator (100 mW/cm 2)	_	_	0.1M Na_2S + 0.02M Na_2SO_3 (pH = 12.7)	≈80 µ mol h^{-1} cm^{-2}	[72]
NiS NPs/CdS NPs/TiO_2 Nanosheets	One-step sulfurization	300 W Xe lamp, λ > 420 nm	_	50 mg	0.25M Na_2S + 0.35M Na_2SO_3	2149.15 µ mol $h^{-1}g^{-1}$	[29]
Ni_2P/CdS	Hydrothermal method and solvothermal method	300 W Xe lamp, λ > 420 nm	_	5wt% Ni_2P/CdS	1.5 M as $(NH_4)_2SO_3{\cdot}H_2O$	58mmol h^{-1} g^{-1}	[73]
CdS/Ni_3S_2	_	300-Watt Xe lamp, λ > 420 nm	_	_	0.5M Na_2S + 0.5M Na_2SO_3	178µmol·cm^{-2}·h^{-1}	[74]
$LaFeO_3$/CdS/CQD	Hydrothermal method	Sun light illumination	_	10mg	Lactic acid	25,302µmolh^{-1} g^{-1}	[75]

CdS@CdSe-MoS2	Precipitation method	300 W Xe-lamp	_	10mg	Lactic acid	4850 $\mu molh^{-1} g^{-1}$	[76]
ZnO/CdS	_	350 W Xe lamp	_	50mg	Na_2SO_3 and Na_2S	4134 $\mu molh^{-1} g^{-1}$	[77]
CdS/Graphdiyne	In situ growth process	Blue LED light	_	2mg	Triethanolamine	4100 $\mu molh^{-1} g^{-1}$	[78]
Pt-TiO_2/CdS	Precipitation method	Xe-lamp (λ>420 nm)	_	100mg	_	3.074 $\mu molh^{-1} g^{-1}$	[79]
Bi-doped carbon QDS/CdS	Solvothermal method	300-Watt Xe-arc lamps	_	50mg	Na_2S and Na_2SO_3	1770 $\mu molh^{-1} g^{-1}$	[80]
$PbTiO_3$/CdS	Ultrasonication	300 W Xe lamp illumination	_	_	Na_2S/Na_2SO_3	849.0$\mu mol\, h^{-1} g^{-1}$	[81]

2.2 Cadmium sulfide/MOF based hybrids for photocatalytic water splitting

MOF is a highly porous and crystalline structure material with huge surface area for reaction and high stability. The CdS/MOF have many advantages over conventional single catalyst for H_2 production. They take advantages of both favorable properties of CdS and MOF. The CdS have great potential for harvesting solar energy and MOF provide better dispersion of CdS and give stability, well charge separation, and stop the recombination of charges (electrons-hole pairs) and form heterojunctions for H_2 production. CdS/MOF is materials which have narrow band gabs (E_{bg}<3) and suitable for H_2 production. It is also noted that VB (valance Band) is more positive side on top then oxidation potential to produced O_2 conduction band on more negative than reduction potential. Under visible light irradiation MOFs enhanced the photo catalytic activity of CdS [16, 82]. In a study, for high efficiency and stability, CdS catalyst are deposited on UiO-66 MOF. Pure CdS may tend to aggregate together and active sites are reduced for water-splitting, crystal of pure UiO-66 in well-defined octahedral shape and sharp corner gives large surface area for CdS deposition [83]. In another research work by Zhou et al. reported CdS/UiO-66 prepared via hydrothermal method. The fabricated photocatalyst exhibited two times higher H_2 production rate then pure CdS. This is due to excellent dispersion of CdS on UiO-66 (CdS 10 nm) as it acts as an excellent electron acceptor and enhanced charge separation. The optimum H_2 production rate of 235μmole/hr[84]. In 2018, Xu et al. published research on CdS/UiO-66 hybrids, which showed considerably higher activity toward photocatalytic H_2 generation than pure CdS. The application of MOF improves CdS dispersion while also increasing the number of active and sorption sites. Furthermore, transfer of electrons from exciting CdS to MOF resulted in greater electron and hole separation by electrons positioned at UiO-66 and holes in the valence band of CdS, reducing charge recombination and, therefore, increasing photocatalytic H_2 generation productivity

. Figure 3 shows the relationship between H_2 evaluation rate and CdS concentration, as well as varied catalyst concentrations. Due to the perforable development of heterojunction between CdS and UiO-66(10), the CdS/UiO-66(10) initially displays a high H_2 generation rate[85].

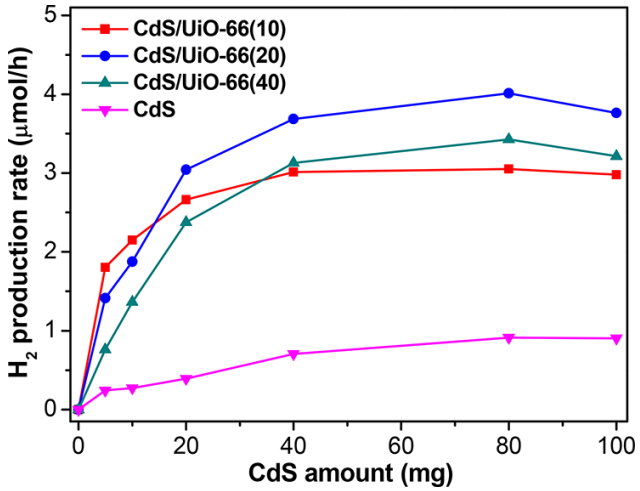

Figure 3: Show H_2 production at different rate of CdS loading. Reprinted with consent [88]. Exclusive Copyrights 2018 ACS.

Mao et al. worked on CdS/ UiO-66-$(SH)_2$ as they introduced thiol-linkage among CdS quantum dots and MOF enhanced the charge separation and transfer for photocatalytic H_2 production. The prepared photocatalyst acted as a functional support and porous medium to anchor CdS quantum dots between 0.5-3 nm in size. The thiol bridge between UiO-66 and CdS shows some remarkable and well-organized transfer of charges carriers, effectively enhancing the transfer process at interface of photogenerated electrons and in under irradiation of visible light (λ > 420nm). The optimized hybrid (UiOS-CdS) displayed a 153.2 $\mu molh^{-1}$ of photocatalytic H_2 evolution. When CdS is incorporated into UiO-66, the H_2 production rate of exceeds to 153 $\mu molh^{-1}$. Furthermore, when the amount of CdS is increased it shows some decline in the production rate of H_2 due to block the channels of MOF shown in figure 4b. The apparent quantum efficiency of the UiOS-CdS0.7 was determined at 380nm and 420nm and it show slightly increase in the efficiency i.e. 14.8% and 11.9% respectively shown in figure 4c. UiOS-CdS0.7 showed stability in consecutive four cycle without significant change in activity shown in Figure 4d [86].

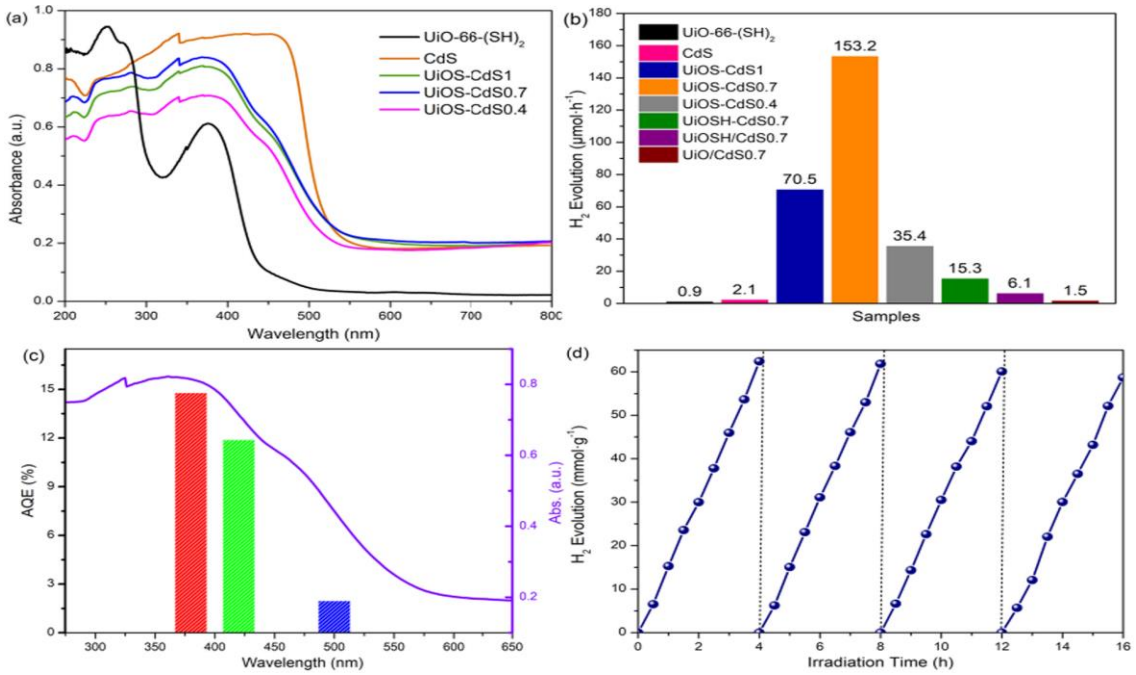

Figure 4: UV-vis absorption and (b) the efficiency of these samples for photocatalytic H_2 evolution (10 mg catalyst); (c) wavelength dependent AQE of H_2 (d) photocatalyst stability. Reprinted with consent [89]. Exclusive copyrights 2020 Elsevier.

Guo et al. manufactured an efficient heterojunction photocatalyst CdS/Ni-MOF. The creation of a hybrids demonstrates that at an optimal 40 percent loading of CdS, it produces 2508 molh-1g-1 of H_2. Furthermore, Ni-MOF are important in trapping the electrons on CdS [87]. He et al. fabricated CdS supported on MIL-101 for photocatalytic splitting of water by the irradiation of visible as well as UV light. It was observed that no significant H_2 production takes place when pure MIL-101 is used but when loaded with 5% CdS (on MIL-101) the hydrogen production reached to 4440 μ mol $g^{-1}h^{-1}$ [88].

Table 2 CdS/MOF-base Hybrid Catalyst for Photocatalytic H_2 Production

Catalysts	Central metal for MOF	Experiment Conditions	Stability of catalyst	H_2 production rates	Ref.
Au-CdS/MIL-101	Chromium	Catalyst:10mg, water:100ml, Na_2S and Na_2SO_3 20 mmol, 300-watt Xe lamp,λ>420nm.	No loss of catalyst activity with continue four cycles	25000 µmole $h^{-1}g^{-1}$	[89]
PTC-CdS/MIL 101	Chromium	Catalyst:15 mg, Na_2S and Na_2SO_3 20 mmol, 300-watt Xe lamp,λ>420nm	No loss of catalyst activity after 3 cycles, also there is no changed in XRD patterns after experiments. .	13139 µmole $h^{-1}g^{-1}$	[90]
CdS/UiO-66	Zr	Catalyst:5mg, Ascorbic acid:20mmol (0.1 M) solution, Pt:0.5wt%,300-watt Xe lamp,λ>420nm	No such evident found in decrease in H_2 evolution within 16 hours, also there is no changed in XRD patterns after experiments.	47000 µmole $h^{-1}g^{-1}$	[85]
CdS-MoS_2/UiO-66	Zr	Catalyst:20mg, Lactic acid 80ml with 10% solution, 300-watt Xe lamp,λ>420nm	No loss of catalyst activity after 4 cycles, also there is no changed in XRD patterns after experiments which like fresh catalyst.	32500 µmole $h^{-1}g^{-1}$	[91]
NiS-CdS/TiO_2	MIL-125 (Ti)	Catalyst:50mg, Na_2S and Na_2SO_3:60ml with 0.3 M solution, 300-watt Xe lamp,λ>420nm	Equal amounts of H_2 produced in each five cycles.	2149.1µmole $h^{-1}g^{-1}$	[29]
CdS@TiO_2	MIL-125 (Ti)	Catalyst:50mg, Na_2S-$9H_2O$ (0.2) and Na_2SO_3(0.3 M) :60ml, 300-watt Xe lamp,λ>420nm	After 3 cycle there is No change noted in the H_2 production.	1970.8 µmole $h^{-1}g^{-1}$	[92]
CdS-CoC@Co9S8	ZIF-67	Catalyst:1mg, Lactic acid 3ml with 10% solution, 150-watt Xe lamp. .	There is marginal decrease was observed second cycle.	26690 µmole $h^{-1}g^{-1}$	[93]
CdS/Co_3O_4/Ni	ZIF-67	Catalyst:20mg, Lactic acid 30ml with 10% solution,300-watt Xe lamp,λ>420nm	Equal amounts of H_2 produced in each four cycles	5120 µmole $h^{-1}g^{-1}$	[94]
QDsCdS@MIL-101	Chromium	Catalyst:30mg, Lactic acid 50ml with 10vol% solution,300-watt Xe lamp,λ>420nm	No change in catalyst activity in each 4 Cycle, no change observed in XRD patterns and morphology after 4 cycles.	4886 µmole $h^{-1}g^{-1}$	[28]
UiO-66-(S-CdS)2	Zr	Catalyst:10 mg irradiation of 420 nm light 0.35 M Na2S + 0.25 M Na2SO3	No change in catalyst activity in each 4 Cycle,	153µmol h^{-1}	[95]

2.3 Electrocatalytic applications of CdS and its hybrid for water-splitting.

In electrocatalytic water-splitting, the system consists of an aqueous electrolyte, electrodes, and external circuit. When potential difference is applied between electrodes, it results in evolution of H_2 at cathode and oxygen gas at anode [36, 37]. The OER is slow reaction kinetics and required high potential compared to HER. Moreover, the pH of electrolyte has a big impact on OER, as it works very differently in acidic and basic environments. Oxygen and hydrogen are produced by oxidation two water molecules at a potential of 0.404 V. Electrolysis is commonly carried out in acidic environments with a proton exchange membrane as illustrated in figure-5A to avoid charge transport losses.[96, 97]. It is concluded that water-splitting is easier in alkaline medium compared to acidic medium [98].

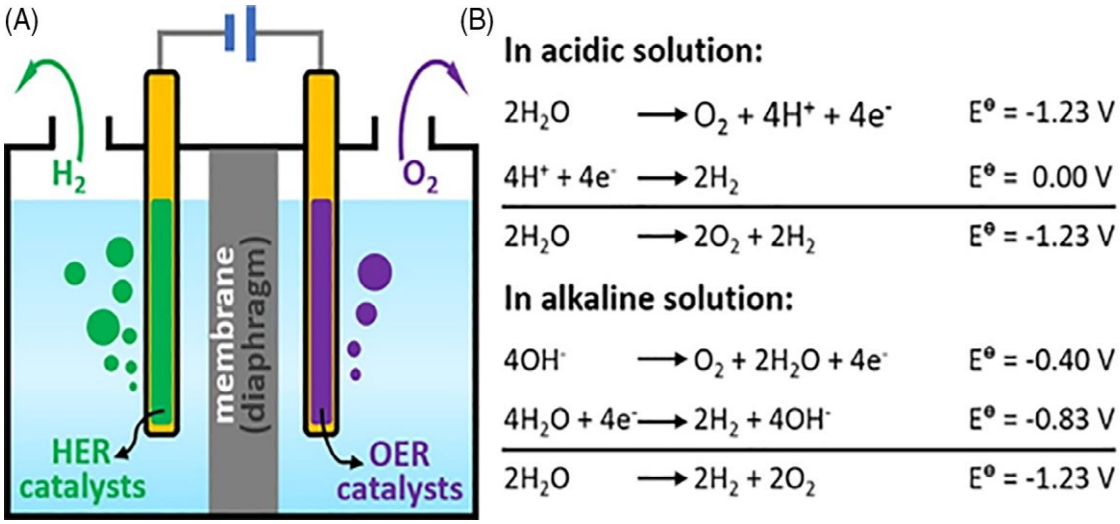

Figure 5: (A) Water splitting via electrocatalytic cell (B) Electrocatalytic reaction in acidic and basic medium. Reprinted with consent [37]. Exclusive copyrights 2018 American Chemical Society.

Fangyuan et.al fabricated CdS/Co_8S_9/Ni_3S_2 hybrid catalyst for effective electrocatalytic water-splitting via hydrothermal process. The self-supported catalyst used very low cost and more active in alkaline medium for both HER and OER. The bi-functional catalyst demonstrated exceptional capabilities, with a low overpotential of 69 mV for HER and 285 mV for OER, respectively, to attain current density of 10 mA/cm^2. The overall water-splitting of the photo-assisted electrocatalyst, which gives 174.1 percent more H_2

output than that of single electrocatalyst [99]. 3D CdS/Ni_3S_2/PNF were designed by Qu et Al. for electrocatalytic water-splitting in alkaline medium. The CdS QDs loaded on Ni_3S_2 nanosheet flowers then CdS/Ni_3S_2. The increased exposure to the active site of nano petalites results in excellent catalytic efficiency. With working electrode using 121 mV potential to achieve current density of 10 mA/cm^2 is used in 1 M KOH [100]. Sheng et al. used the hydrothermal process to fabricated Cobalt doped molybdenum sulfide on CdS nano rods (CdS@$CoMo_2S_4$/MoS_2). The dual advantages of elements Co and Mo increased the active sites and improved the conductivity. Moreover, the MoS_2 edges maximally exposed the interfacial area between the catalyst and electrolyte was improved. The maximum MoS_2 process shows an improved 46.60 μmol/g.h of H_2 production rate [101]. Garg et al. manufactured CdS deposited on the surface of Transition Metals (TMs) for electrocatalytic water-splitting. It was found that TM/CdS nanotube were very stable with high catalytic activity towards HER and OER. Most TM@CdS NTs were efficient in decreasing the OER overpotential compared to bare CdS nanotubes. Pd@CdS NT demonstrated the best activity and reduced the OER overpotential compared to other TMs due to less OER intermediate interaction with Pd@CdS NTs surface[102].

Wei et al. presented CdS modified with In_2S_3 and cocatalyst NiO-OH. It was observed that as prepared catalyst showed a 1 mA/cm^2 photocurrent density at 1.23 V vs. RHE indicating that In_2S_3 significantly enhanced photogenerated carrier separation efficiency, while NiO-OH act as protection against photo corrosion[103]. Yu et al. developed a heterostructure structure out of homogenous Zn-doped CdS/TiO_2. The modified catalyst demonstrated higher PEC efficacy with a 3 mA/cm^2 photocurrent density at 1.23 V vs RHE, by modifying the thickness of ZnO and deposition duration of CdS. The increased activity can be attributed to improved charges transportation and separation ability, increased light absorption, and increased photoactivity. [104].

Chapter 3

Material and Methods

3.1 Materials

The analytical grade chemicals utilized in the production of CdS-NRs hybrids with PBNPs were acquired from Sigma Aldrich. Potassium hexacyanoferrate trihydrate ($K_4[Fe(CN_6).3H_2O]$, Ethylenediamine (EDA), Cadmium nitrate tetrahydrate ($Cd(NO_3)_2.4H_2O$), Thiourea, Ethanol, Hydrochloric Acid (HCl), and deionized water were among the chemicals used.

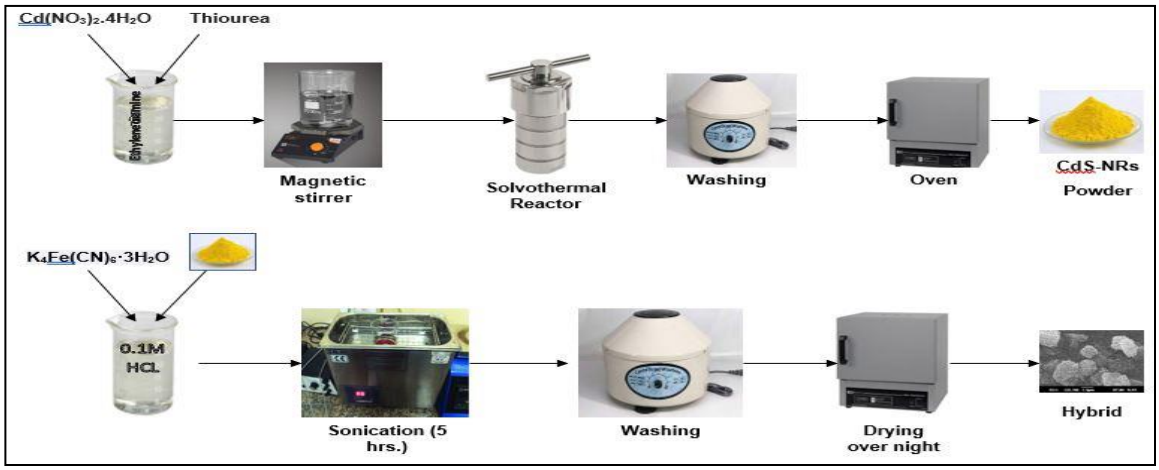

Figure 6: Schematic diagram of synthesis of CdS-NRs and hybrid based electrocatalyst

3.2 Preparation of Pure CdS

The CdS micro/nano rods were manufactured using the solvothermal process. Cadmium nitrate tetrahydrate 3.088g (10 mmol) and thiourea 1.52g (20 mmol) were measured and dissolved in 50 mL ethylenediamine (EDA) with continuous stirring. After 30 minutes of stirring, the mixed solution was placed in a Teflon-lined autoclave and heated at 200°C for 14 hours. The resulting product was centrifuged, then rinsed with deionized water several times before being cleaned with ethanol. It was then oven dried for 12 hours at 80°C before being used for further research.

3.3 Preparation of Pure Prussian Blue (PBNPs)

In a typical process, 2 mmol of Potassium hexacyanoferrate (II) trihydrate ($K_4[Fe(CN_6).3H_2O]$ was put in 100mL of HCl (0.1M). The solution was ultrasonically maintained at 40°C for 8 hours. The blue product was collected and cleaned in ethanol and deionized water. The product was dried overnight in a vacuum oven at 40°C.

3.4 Preparation of Hybrids of CdS-NRs@ PBNPs

CdS was dissolved in 100 mL HCl (0.1M) solution. Potassium hexacyanoferrate (II) trihydrate ($K_4[Fe(CN_6).3H_2O$) was then introduced, and the solution was ultrasonically kept at 40°C for 8 hours. The final product was obtained and washed with deionized water before being dried in a vacuum oven at 60°C overnight. A fixed quantity of CdS was combined with varying ratios of $K_4[Fe(CN_6).3H_2O$) to produce distinct product compositions such as 1:1, 1:2, and 1:3.

3.5 Characterization and Electrochemical Study

X-ray diffraction (XRD) (STOE-SEIFERTX'PER PRO) was used to evaluate the crystallinity and compositional analysis of the as-fabricated catalysts. The SEM used to analyze structure and surface morphology coupled with EDX. The FTIR techniques used to obtain infrared absorption spectrum of powdered materials to identify the functional group in catalyst. Ink was prepared for the electrochemical study of the catalyst. 1 mL of NMP and 2.5 mg of PVDF were mixed for 30 mins. After that 42mg of active catalyst and 5mg of carbon black were introduced to the mixture and stirred for one hour. The resulted suspension was sonicated for 4 hours, the final solution was drop casted on the both side of Ni-foam and finally dried at 60°C for overnight. Electrochemical analysis has been carried out on a Gamry potentiostat with a three-electrode configuration. Nickel foam-based electrodes were employed as working electrode, whereas reference and counter electrodes were Ag/AgCl and Pt wire, respectively. In a 1M KOH solution, the catalytic activities of these electrodes were investigated at varied scan speeds. For ease of computation, standard Reversible Hydrogen Electrode (RHE) potential was calculated using equation (1).

$$E_{RHE} = E_{Ag/AgCl} + 0.059PH + 0.1976 \quad \text{Eq.21}$$

Chronopotentiometry tests were done for 86400s to assess the stability of the prepared catalyst. An Alternating Current (AC) voltage of 10 mV was used to conduct electrochemical impedance spectroscopy (EIS) across a frequency range of 200 kHz-100mHz. Eq.21 was used to compute the electrochemical active surface area.

$$ECSA = C_{ò} / C_s \quad \text{Eq.22}$$

Where $C_{ò}$ represents doubled layer capacitance and Cs represents flat surface specific capacitance per unit area, with a suitable range of 0.040 $mF.cm^{-2}$.

Chapter No 4

Results and Discussion

4.1. Characterization of CdS-NRs@PBNPs based different electrocatalysts

4.1.1. X-ray diffraction analysis

Powder X-ray diffractometry was used to determine the crystalline phases in the synthesized catalyst. Figure-7(a) illustrates XRD spectra of CdS-NRs. The spectra correspond to the crystal planes of hexagonal CdS-NRs (JCPDS card 41-1049). Peaks were indexed at planes (100), (002), (101), (102), (110), (103) and (112) matching the diffraction peaks at 2θ values of 24.8, 26.5, 28.1, 36.6, 43.6, 47.8 and 51.8 respectively. The XRD spectrum of PBNPs is shown in Figure-7(b). The peaks at 2θ = 17.5, 24.7, 35.4, 39.8, 43.7, 50.7, 54.2 were attributed to the PB planes (200), (220), (400), (420), (422), (440), and (600), indicating that PBNPs was synthesized (JCPDS 73-0687). The face-centered cubic phase of PBNPs can be used to index all these reflections. XRD patterns of hybrid CdS-NRs@PBNPs(1:1), CdS-NRs@PBNPs(1:2), and CdS-NRs@PBNPs(1:3) are shown in figure-7(c, d) and figure-7(e). The planes (1 0 0), (1 0 1) and (110) crystal planes of CdS can be well detected as the three primary peaks for all the hybrids at 24.8, 28.1, and 43.7 respectively suggesting no crystal structure change after the PBNPs modifying the surface of the CdS-NRs[105]. The (100) plane of CdS-NRs appear as shoulder peak of (220) plane of Prussian blue because both peaks almost same position. The all planes of PBNPs appears in all three hybrids as strong peaks. X-ray line broadening was used to calculate the average crystallite size of nanocomposite, which was using Scherrer's equation [106].

$L=(k.\lambda)/(FWHM)(\cos\theta_B)$

L=crystallite size

K=shape factor . λ=X-ray wavelength

FWHM=Full width at half max θ_B=Bragg angle

The average crystallite size CdS-NRs, PBNPs, CdS-NRs@PBNPs(1:1), CdS-NRs@PBNPs(1:2), CdS-NRs@PBNPs (1:3) is 274Å (27. nm), 363Å (36.3nm), 342.71Å (34 nm), 416 Å(41.6nm) and 401Å(40.1nm) respectively.

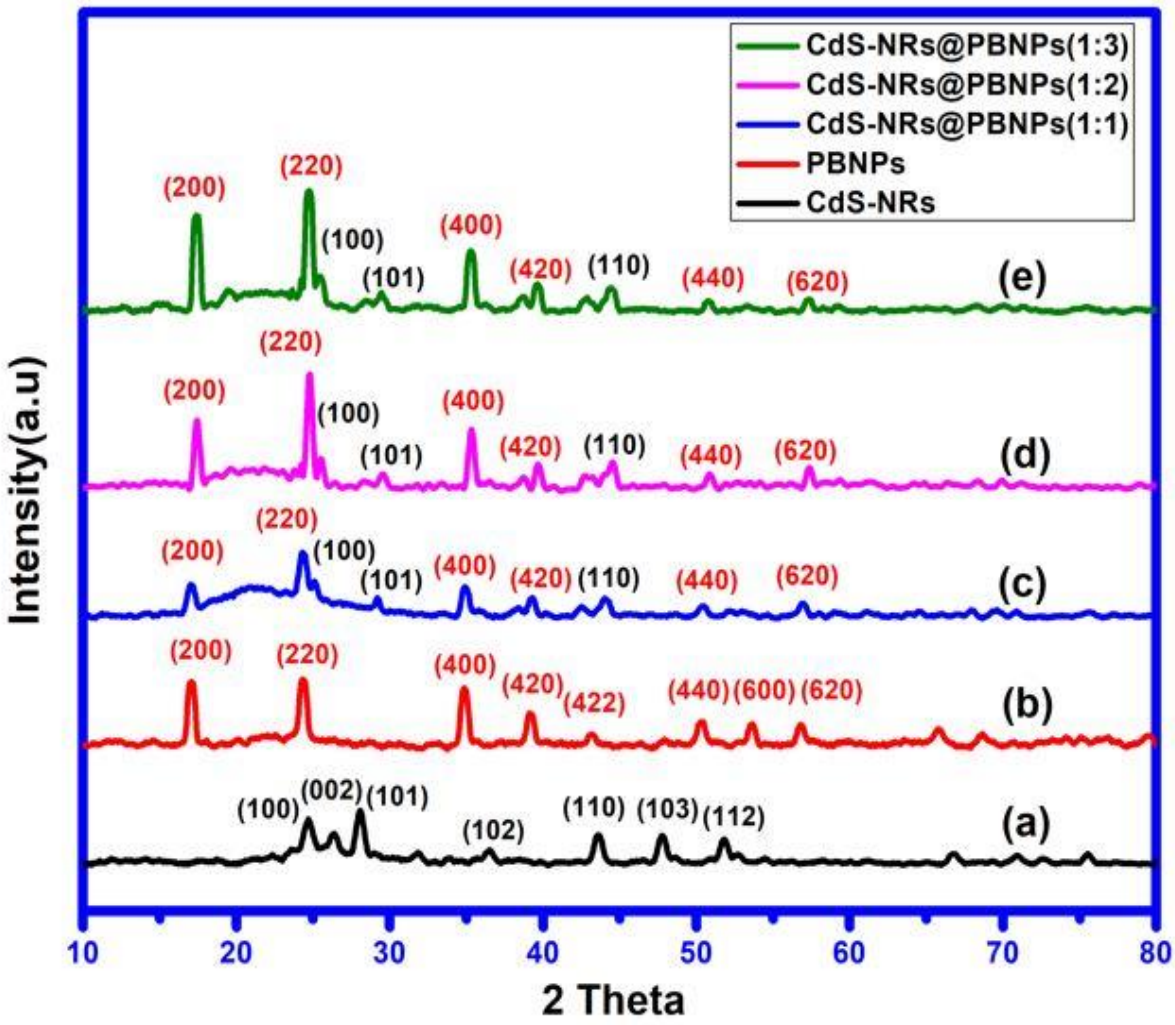

Figure 7: XRD pattern of **(a)** CdS-NRs **(b)** PBNPs **(c)** CdS-NRs@PBNPs(1:1**) (d)** CdS-NRs@PBNPs(1:2) **(e)** CdS-NRs@PBNPs(1:3)

4.1.2 Fourier Transform Infrared Spectroscopy (FTIR)

FTIR spectra obtained in the range of 500 cm^{-1} to 4000 cm^{-1} are given in Figure 8. KBr medium was used to prepare the samples. The FTIR spectra of pure CdS-NRs is shown in Figure 8A. The strong absorption band detected at 623 cm^{-1} is caused by CdS-NRs

stretch vibrations [107]. The bending vibration maxima of water molecules can be detected at 1627 cm ^{1}. The broad peaks at 3420 cm^{-1} correspond to the broad O–H vibrations of water molecules [108]. Strong absorption bands revealed traces of SO peaks at approximately 1120 cm $^{-1}$ [109]. In addition, the peaks at 660 and 1120 cm^{-1} can be attributed to the Cd-S bond [110]. The prominent peak at 2075 cm^{-1} is PBNPs characteristic peak, and it can be because of CN stretching in the [Fe–CN– Fe] units [111]. A stretching band at 2084 cm^{-1} was detected in the FTIR spectra of PBNPs, which was attributed to the usual CN bond of the PBNPs crystal. The characteristics peak 623 cm^{-1} of CdS-NRs is observed with absorbance peak of PBNPs which can also be seen in hybrids. The characteristics peaks 1120 cm^{-1} due to Cd-S stretching vibration clearly absorbed as a sharp peak in CdS-NRs@PBNPs (1:1) and CdS-NRs@PBNPs (1:2) hybrids and medium peak in CdS-NRs@PBNPs(1:3). The characteristics peak of PBNPS at 2075 cm^{-1} is also present in all hybrids as strong and sharp peak.

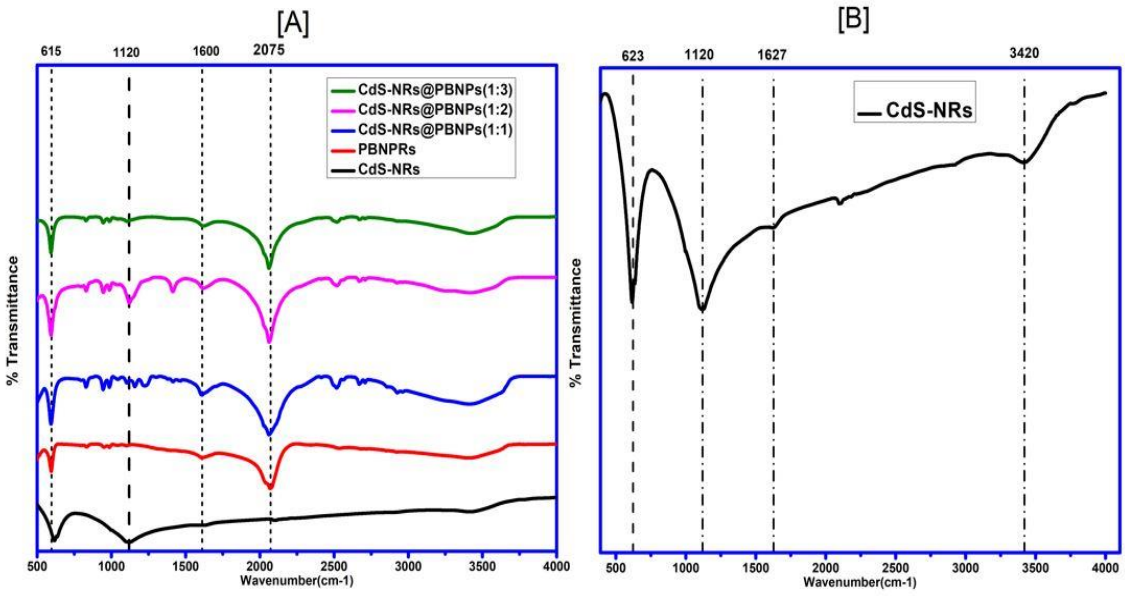

Figure 8: FTIR of **(A)** CdS-NRs, PBNPs, CdS-NRs@PBNPs(1:1), CdS-NRs@PBNPs(1:2) and CdS-NRs@PBNPs(1:3) **(B)** pure CdS-NRs.

4.1.3 SEM and EDX

SEM was used to analyze the morphology of CdS-NRs and their hybrids samples; SEM are shown in Figure 9. The development of rod-like structure with uniform size and smooth surface is observed in CdS-NRs as shown in Figure 9A.

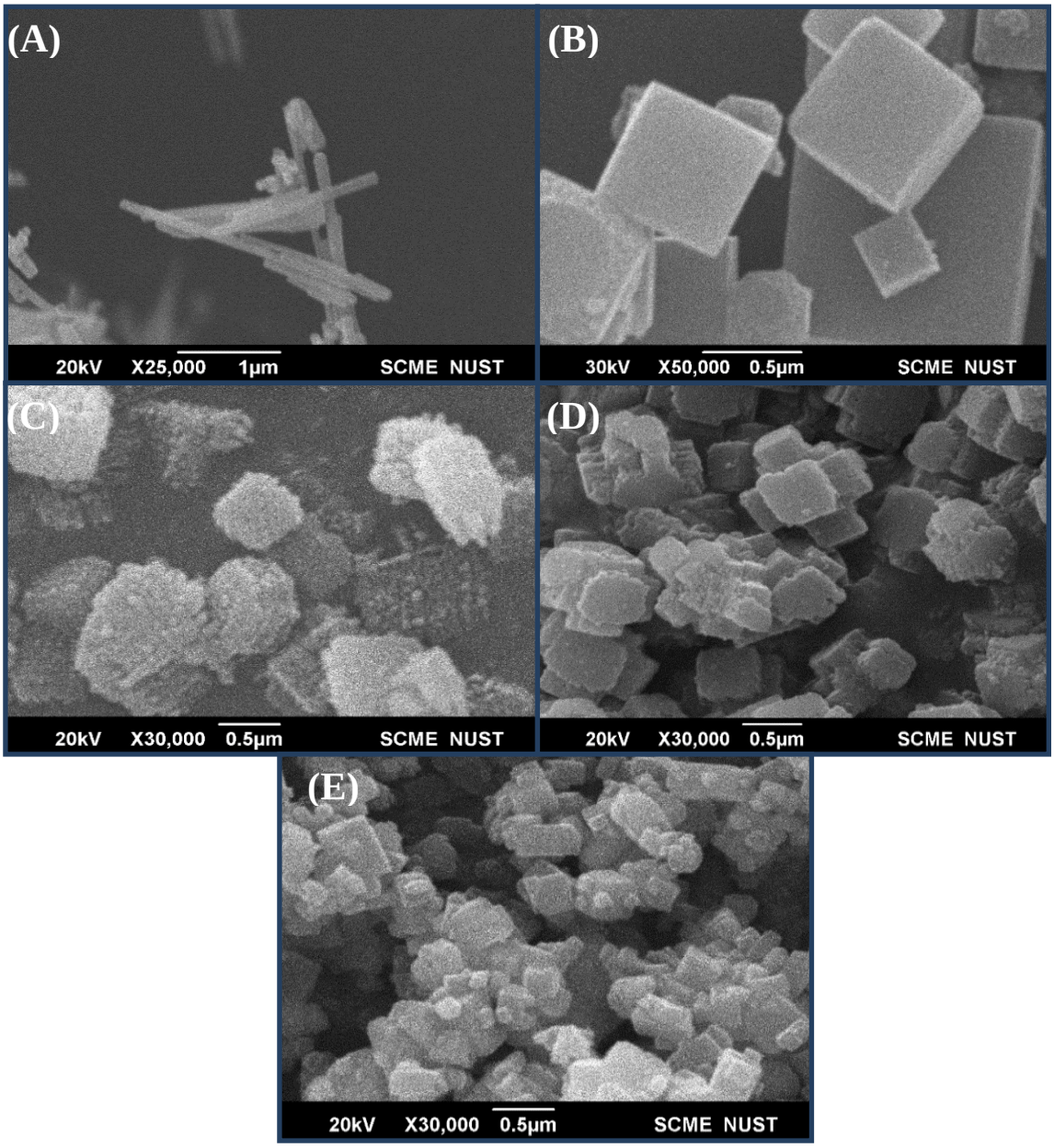

Figure 9: SEM image of (A) pure CdS-NRs, (B) pure PBNPs, (C) CdS-NRs@PBNPS(1:1), (D)CdS-NRs@PBNPS(1:2) and (E)CdS-NRs@PBNPS(1:3)

The structural information of PBNPs obtained from SEM images shows uniformly well-formed cubes as shown in Figure 9B which was similar to reported PBNPs [112].A magnified SEM image displays a remarkably smooth surface over the whole particle,

indicating that the PB nano cubes are single-crystal-like. The original PBNPs microcrystals' particle-size distributions were quite narrow. In significantly magnified SEM pictures, very rough textures were found at the edges of the cubes, revealing that the cube forms were created by agglomeration of tiny PB nanocrystals[113]. CdS-NRs are distributed very smoothly over the surface of PBNPs in hybrid (1:1), and as the ratio increases in hybrids (1:2, 1:3), CdS-NRs are dispersed in PBNPs surfaces and the corner of PBNPs is somewhat broken.

The main elemental compositions of the CdS-NRs@PBNPs (1:1) hybrid include Cd, S, Fe, N, and C, according to the EDS spectrum (shown in Figure 10A, B). Furthermore, the distribution of Cd, S, and iron components in the hybrid material is quite homogeneous, suggesting that CdS-NRs and PBNPs have been integrated together successfully. The results show that the elements in the hybrid are evenly distributed and in proximity. The aforesaid semiconductor materials' excellent recombination will make charge separation and transfer faster, improving the composite's electro catalytic performance even further. The CdS-NRs@PBNPs EDS spectrum also demonstrates that hybrids were successfully developed, with the atomic percentages of Cd, S, Fe, N, and C in the being 31.93%, 0.12%, 13.43%, 27.63%, and 26.89%, respectively.

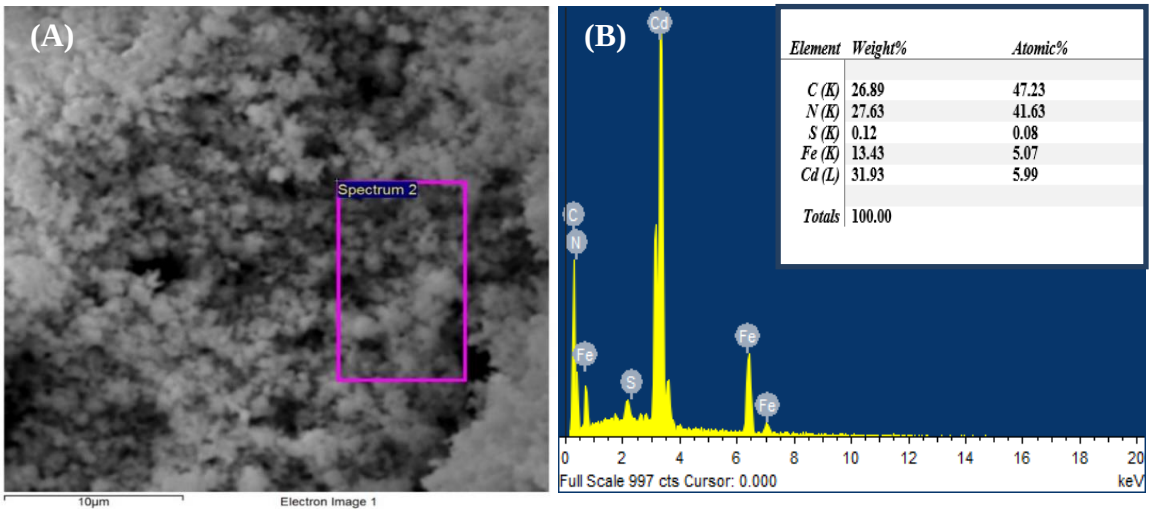

Figure 10: (A) SEM top image with EDS area mentioned (B) the corresponding elemental analysis spectrum of CdS-NRs@ PBNPs(1:1) hybrid

4.1.4 BET

Figure 11 depicts the BET (Nitrogen adsorption-desorption isotherms) of CdS-NRs@PBNPs(1:1). The catalyst was extensively dried before the measurement by heating it at 50 °C overnight under vacuum. Degassing was performed at 50°C for 24 hours. This temperature was used to prevent the structure from collapsing. The material clearly demonstrated a Type IV sorption isotherm, which is typical of mesoporous materials. Using the BET model, the surface area calculated was 96.62 $m^2.g^{-1}$ and the pore volume was 0.124 $cm^3.g^{-1}$. It is noteworthy that the surface area is exceptionally large, well above the estimates of 49.7 $m^2.g^{-1}$, 35.7 $m^2.g^{-1}$, and 28.7 $m^2.g^{-1}$ for dehydrated Prussian blue, Prussian blue meso-crystals, and PAN/PBNPs respectively [114-116]. This finding implies that the adsorption occurs primarily on external surface of the nanoparticles and the cavity between the consecutive particles creates a system of mesoporous channels with dimension between 10 and 20 nm [39]. As a result, the insertion of PBNPs significantly improves the surface area and sufficient redox reactions for the CdS-NRs@ PBNPs (1:1) electrocatalyst.

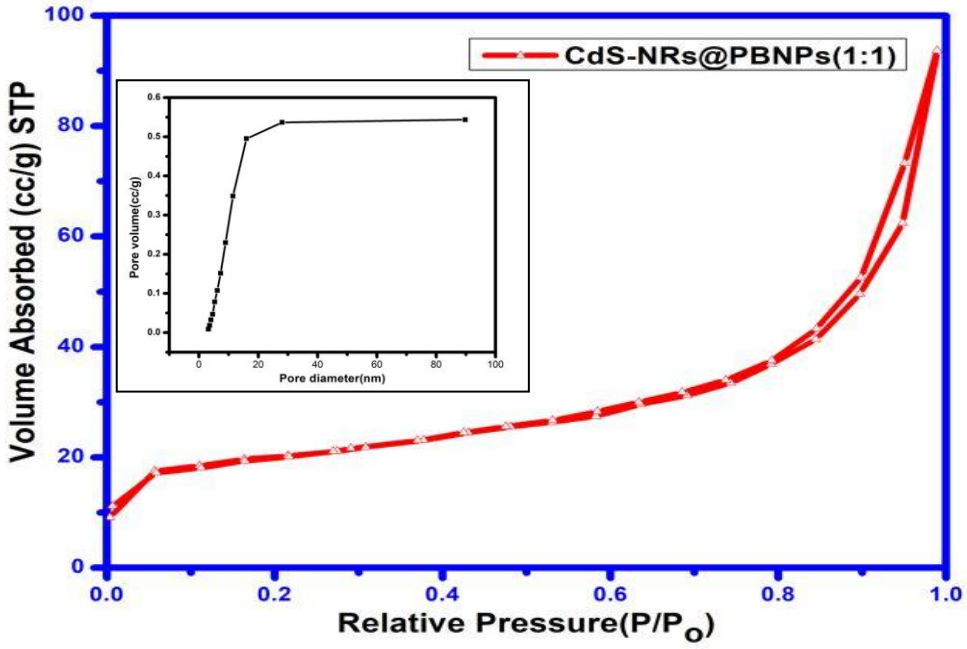

Figure 11: N_2 Adsorption and desorption isotherm of CdS-NRs@PBNPs(1:1).

4.2 Hydrogen Evolution Reaction (HER)

A three-electrode setup is used to measure the electrochemical properties of pure CdS, PBNPs, and their hybrids in a 1 M alkaline solution. The samples' HER activity is assessed using linear sweep voltammetry curves as explained in Figure 12A. In comparison to pure CdS and PBNPs, the hybrids demonstrated better HER activity. Pristine CdS and PBNPs has a reported overpotential of 197 mV and 188 mV at a current density of 10 $mA.cm^{-2}$. This showed the presence of cadmium in the catalyst increases the activity of HER. The hybrids with CdS-NRs@PBNPs(1:1), CdS-NRs@PBNPs(1:2) and CdS-NRs@PBNPs (1:3) have overpotentials of 126 mV, 137 mV, and 178 mV, respectively at current density of 10 $mA.cm^{-2}$. In comparison to the other hybrids, the CdS-NRs@PBNPs (1:1) has the least overpotential of 126 mV at a current density of 10 $mA.cm^{-2}$. As a result of having characteristics and an electrical configuration like noble metals, CdS is the active site for HER. The number of active sites in the nanocomposites (CdS-NRs@PBNPs) and the compact heterojunctions among CdS-NRs and PBNPs are attributed to the increased electro catalytic hydrogen generation. This increase might be attributed to more active edge sites on the CdS nanorod surface, which prevent charge carrier recombination and rapid charge carrier migration, resulting in improved electro catalytic H_2 generation.

Furthermore, the CB potential of PBNPs is closer to that of CdS-NRs, resulting in quicker electron movement. Another key finding is that having more active edge sites improves proton adsorption, which leads to the production of H_2 via reduction. Tafel slopes are displayed according with Tafel equation to further examine the catalytic performance and kinetics of the hybrids for HER[117].

$$\dot{\eta} = ƀ \log j + \alpha$$

Here, $\dot{\eta}$= is overpotential, ƀ= is Tafel slope, α= Tafel constant and j=current density.

In principle, the lower the Tafel slope, the greater the catalysts HER activities. The Tafel slope of CdS-NRs@ PBNPs (1:1) is around 157 $mV.dec^{-1}$, which is significantly lower than the other manufactured catalyst utilized in this work, as shown in Figure 12B. Pure CdS-NRs, PBNPs, and CdS-NRs@ PBNPs (1:2 and 1:3) had a Tafel slope of 245, 234, 191, and 160 $mV.dec^{-1}$, respectively.

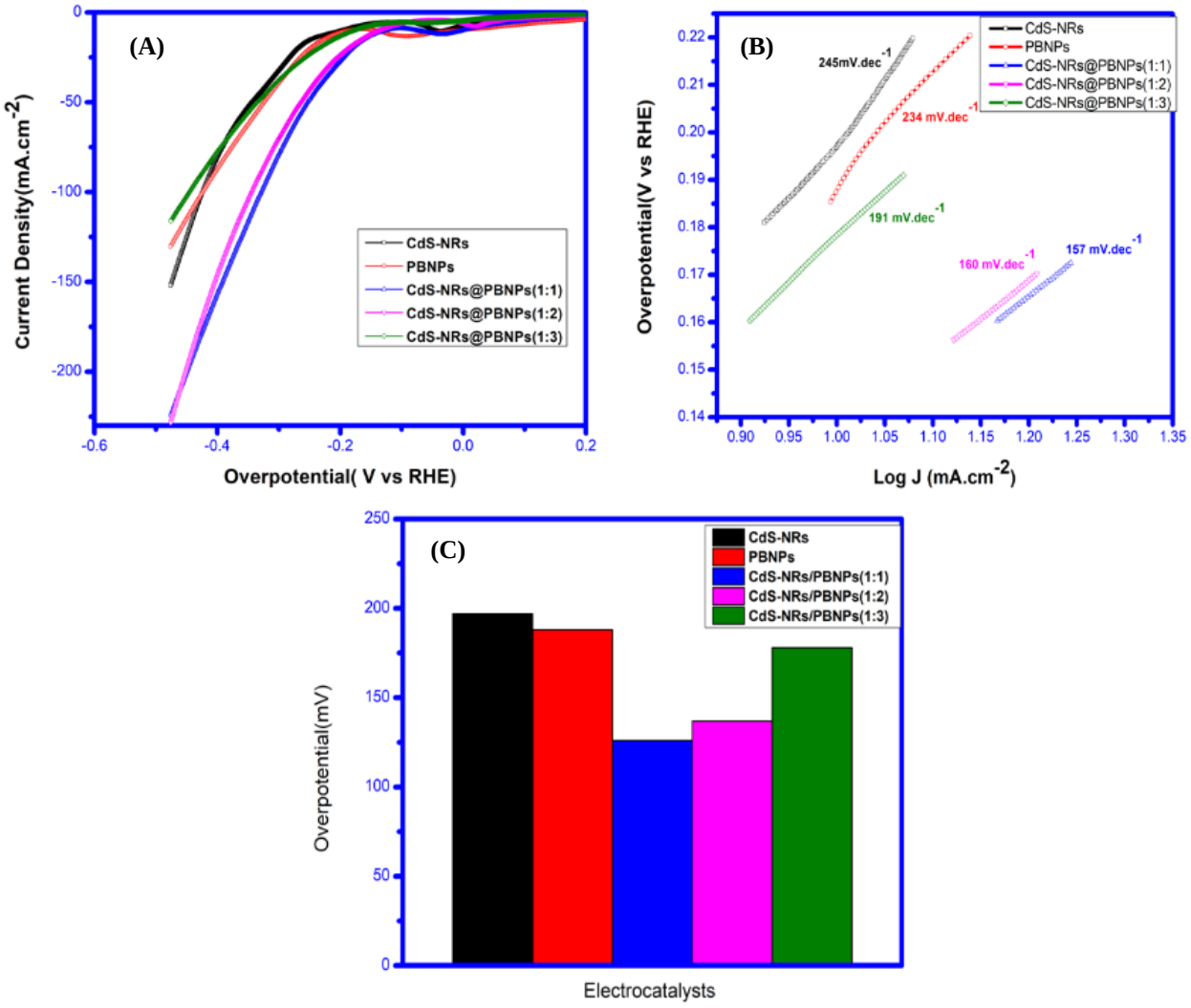

Figure 12: (A) LSV HER curves of pristine CdS-NRs, PBNPs ,CdS-NRs@ PBNPs(1:1, 1:2, 1:3) **(B)** Corresponding TAFEL plots of pristine CdS-NRs, PBNPs ,CdS-NRs@ PBNPs(1:1, 1:2, 1:3) **(C)** Overpotential required for HER

Furthermore, the PBNPs hybrid has a smaller Tafel slope, indicating that CdS-NRs@ PBNPs (1:1) has distinct kinetics than the other electrocatalysts. The Volmer-Heyrovsky step's kinetic mechanism follows 4-5 [118].

Volmer step:

$$H_2O + M + e^- \longrightarrow M - H_{ads} + OH^{-1} \qquad \text{Eq.23}$$

Heyrovsky step:

$$H_2O + M + - H_{ads} + e^- \longrightarrow H_2 + OH^{-1} \qquad \text{Eq.24}$$

The adsorption sites are denoted by the symbol 'M'. The H_2O molecules discharge in the alkaline medium on the catalyst surface, results in the formation of an intermediate of adsorbed hydrogen. Previous research has demonstrated that CdS hybrids enhance water dissociation well because to their large surface area, making them favorable for the alkaline HER process. The exceptional performance of PBNPs hybrids, such as CdS-NRs@ PBNPs (1:1), is owing to a synergistic interaction between PBNPs nanoparticles and CdS, as well as the conductive support given by Ni foam. As a result, the hydrogen adsorption is increased, resulting in an excellent electrocatalyst performance. By developing a narrow pathway, Ni foam offers mechanical stability as well as facilitating the movement of the ions it toward the active sites. The catalyst's strong HER performance is due to the nano particles of CdS that have increased exposure to the active sites. Furthermore, the Fe and N components can change the electronic structure of Cadmium and sulfur, resulting in increased HER performance. **Table-3** compare some efficient catalysts for HER from the literature.

Table 3 Different reported catalyst for HER

Sr. No.	Catalysts	Reaction type	Current density(mA.cm^{-2})	Overpotential (mV)	Tafel slope (mV.dec^{-1})	Stability (hours)	Ref.
1	**CdS-NRs@PBNPs(1:1)**	HER	10	126	157	20	This work
2	**Phosphorene quantum dot@PBNPs**	HER	10	148	79	-	[119]
3	**Ni–Co PBA**	HER	10	215	72	10	[120]
4	**CdS/NI3S2/PNF**	HER	10	121	110	12	[100]
5	**PB-Co@Co-N-PHCS**	HER	10	183	114	24	[121]

4.3 Oxygen Evolution Reaction (OER)

Advanced catalytic kinetics investigated using electron transfer mechanisms in basic media for OER. The OER efficiency of the generated electrode material in a 1M alkaline was investigated using LSV polarization curves (Figure 13A). At a current

density of 10mA/cm^2, the CdS-NRs@ PBNPs (1:1) had the least overpotential of 250mV and overpotential of 316 mV at a current density of 20 mA/cm^2.Compared to Pure CdS-NRs, PBNPs, CdS-NRs@ PBNPs (1:2, 1:3) which required overpotential 319, 350, 270, 308 mV respectively; CdS-NRs (1:1) has a significantly lower overpotential. Because of the conductive properties of CdS and iron, charge transfers are promoted during electrochemical processes. The Tafel slopes of CdS-NRs, PBNPs, and their hybrids CdS-NRs@ PBNPs (1:1, 1:2, 1:3) are 138mV dec^{-1}, 191 mV dec^{-1}, 81 mV dec^{-1}, 115 mV dec^{-1} and 117 mV dec^{-1} respectively, as displayed in Figure 13B.

The Tafel slope of CdS-NRs@ PBNPs(1:1) is smaller than pure CdS-NRs, PBNPs, [122]. The finding suggests that equal proportion loading of both CdS-NRs and PBNPs is a more viable and efficient approach of improving catalytic performance. The Tafel slope of pristine CdS-NRs reflects the hydroxyl ions poor adsorption rate on its surfaces. The OER kinetics are accelerated by a lower Tafel value after PBNPs is introduced.

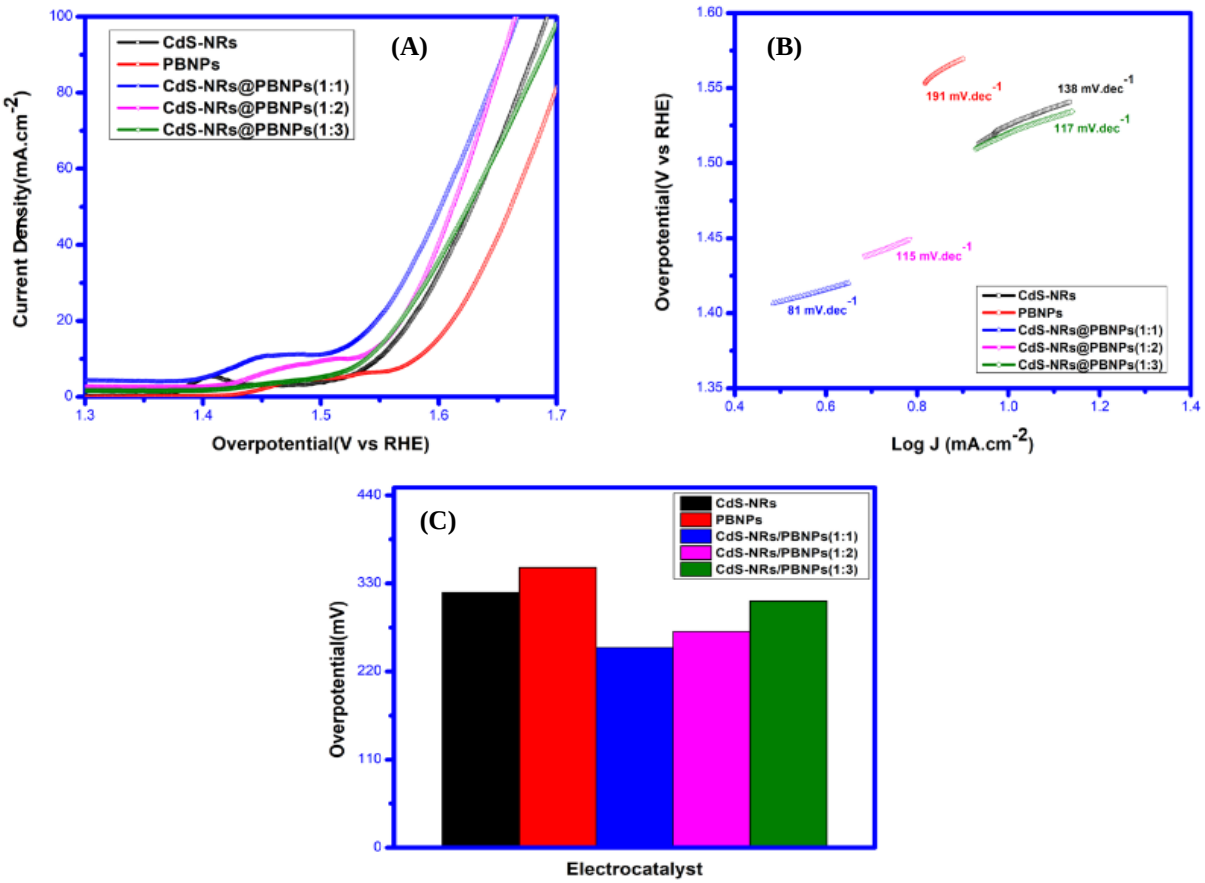

Figure 13:(A) LSV OER curves of pristine CdS-NRs, PBNPs , CdS-NRs@ PBNPs(1:1, 1:2, 1:3).(B) Corresponding TAFEL plots of pristine CdS-NRs, PBNPs ,CdS-NRs@ PBNPs(1:1, 1:2, 1:3), (C) Overpotential required for OER.

The lower Tafel value implies significant OER activity, which is comparable to that of other commercial catalysts. The fact that CdS-NRs@ PBNPs (1:1) has a low Tafel slope indicates that the mechanism is a four-electron process. The rate of the catalyst rises as the potential rise, leading to an increase in electro catalytic efficiency. This notable phenomenon is due to the contact of absorbed oxygen species with the cation sites of transition metals. The heterostructure and interface of Fe and CdS enhances electron transport, resulting in improved electrochemical performance compared to single Fe nanoparticles. **Table 4** compares the different catalysts for OER that have been mentioned in the literature.

Table 4 Different reported catalyst for OER

Sr.no	Catalysts	Current density mA/cm 2	Reaction type	Overpotential (mV)	Tafel plot (mV.dec-1)	Stability (hours)	References
1	**CdS-NRs@PBNPs(1:1)**	10	OER	250	82	20	This work
2	**Mn-CdS@a-Ni3S2**	10	OER	333	192	-	[123]
3	**FeCo-PBA**	10	OER	320	74	20	[124]
4	**Prussian blue/ZIF-67**	10	OER	312	40	-	[125]
5	**CdS/Ni3S2/PNF**	10	OER	280	192	12	[100]

CdS-NRs@ PBNPs (1:1) cyclic voltammetry at varied scan rates from 5 to 50 $mVsec^{-1}$ of applied voltage are shown in Figure 14A. In the potential range of 0–0.6 V, a distinct pair of redox peaks has been observed. Charge is transferred between redox sites via CdS-NRs@ PBNPs (1:1) layers, and ions are transferred through electrode pores, keeping the structure neutral. The essential step that determines the electrode material's reversibility is the adsorption of OH^{-1} at the electrode surface. The profile of the CV stays consistent as the scan rate is increased, demonstrating the catalyst's strong cyclic stability, low resistance, and good electrocatalytic efficacy. By raising the scan

rate, absorber layer impedance is lowered, leading to a high current density. There is a gradual increase in redox peaks as the scan rate rises, indicating that the redox activity is restricted to the surface of CdS-NRs@ PBNPs (1;1), demonstrating the catalyst's stability. Because the pure Ni foam's OER activity is modest, it does not contribute within its potential range. It's merely there to act as a conductive support material [126]. Along with its porous structure, nickel foam creates transmission channels and facilitates the evolution of oxygen and hydrogen.

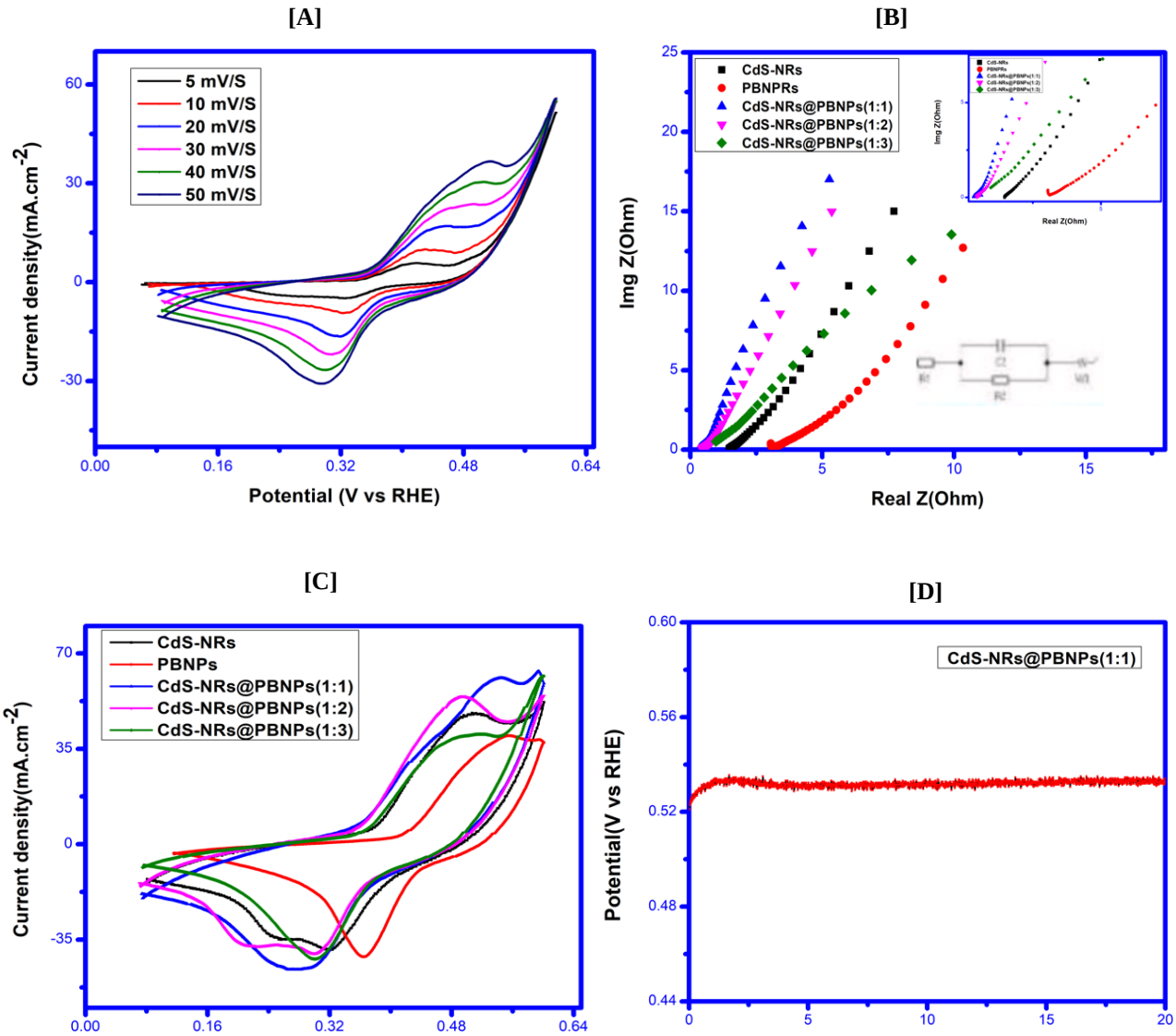

Figure 14: (A) Cyclic Voltammetry of CdS-NRs@ PBNPs(1:1) at scan rate of 5-50 mV.S-1 (B)Nyquist plot at frequency 200kHz-0.1 Hz of pure CdS-NRs, PBNPs, and CdS-NRs@ PBNPS(1:1, 1:2, 1:3) (C) Cyclic Voltammetry curves for CdS-NRs, PBNPs, and CdS-NRs@ PBNPS(1:1, 1:2 and 1:3) **(D)**Stability test of CdS-NRs@PBNPs(1:1) for 20 hours

The strong electrocatalytic activity of PBNPs is attributed to the iron atom presents in the MOF which well-organized cubic structure. This inhibits the nanoparticles aggregation. The inclusion of an appropriate quantity of iron in the Prussian blue matrix is also important. Cadmium has a significant number of active sites. The inclusion of iron and nitrogen in the cubic structure of PBNPs improves electron transport.

As shown in Figure 14B, impedance spectroscopy is employed to further assess the catalytic efficacy of the developed catalyst. In a 1M alkaline media, the testing is done in a range of frequency of 2×10^6 to 0.1Hz. The Nyquist plot is used to match the similar circuit, as seen in the Figure 14B. R_1 represents the impedance of the solutions between the cathode and anode electrodes. The charge transfer resistance is R_2. W is the Warburg resistance that occurs at the electrode and electrolyte interface, and C_2 denotes faradaic capacitance. CdS-NRs@PBNPs(1:1) and other catalysts used in this experiment do not form a semi-circle, indicating that there is no significant charge transfer resistance due to catalysts. CdS-NRs@PBNPs(1:1) resistance line is close to the y-axis, indicating that they behave like super capacitor, indicating that CdS-NRs@PBNPs(1:1) has less Warburg resistance than other catalysts. suggesting a lower Warburg resistance in the electro catalyst It also shows that when the voltage of CdS-NRs@PBNPs(1:1) increases, the Warburg resistance decreases. It's a crucial strategy for electrochemical water splitting. The ECSA of an electrocatalyst is calculated using double layer capacitance, which is a widely known technique of quantification. Another approach for calculating the Cdl value is to utilise electrochemical impedance spectroscopy to compute frequency related impedance. The double layer capacitance was calculated using Eq.25.

$$\dot{C}_{dl}=1/R_1+1/R_2(1/R_1+1/R_2)\,(1/R_1+1/R_2)^{\alpha-1}\}^{\alpha} \quad \text{Eq.25}$$

$$\text{ECSA}=\dot{C}_{dl}/C_s \quad \text{Eq.26}$$

The CdS-NRs@PBNPs (1:1) showed a very high result when the value of Cdl was calculated due to the appropriate ratio of cadmium and iron, which increased the electrocatalyst activity of the catalyst. Eq.26 was used to compute the electrolytic active surface area. CdS-NRs@PBNPs (1:1) had a higher ECSA value of 786.66cm^2, indicating many active sites and increased electron transport.

Table 5 Comparative value of Solution resistance, Charge transfer resistance and ECSA

Catalysts	R_s(ohms)	R_{ct} (ohms)	ECSA(cm^2)
CdS-NRs	0.428	64.09	562.36
PBNPs	0.324	95.8	454.28
CdS-NRs@PBNPs(1;1)	0.013	12.3	786.66
CdS-NRs@PBNPs(1;2)	0.0469	27.25	750.38
CdS-NRs@PBNPs(1;3)	0.428	60.8	666.66

Similarly, the creation of CdS-NRs reduces charge transfer resistance and improves electron transport, resulting in a boost in catalytic activity. Moreover, the catalyst's durability is critical for the commercialization of the concept for hydrogen generation as a fuel. The stability of CdS-NRs@PBNPs (1:1) is tested for 20 hours, as shown in Figure 14D. The catalyst has exhibited a steady behavior based on the chronopotentiometry data, which is attributable to its structural properties. After a swift response, the potential remained steady for the next three hours. The activation of the produced substance during the test is the cause for this. The addition of a nitride layer increased the nanoparticles' stability, preventing them from corroding during HER action. By attracting electrons and producing a rapid electron transfer mechanism, the nitrogen atoms next to the iron atom in Prussian blue promote and enhance the reduction process. The electrode long-term stability evaluation using chrono potentiometry (Fig. 14D) revealed that the catalyst maintains its activity and stability after 20 hours.

Chapter 5

5.1 Conclusions

Even though some incredible advancements have already been accomplished for CdS-based catalysts, yet efforts are still needed to employ CdS-based catalysts for practical and competitive industrial scale applications. To enhance the capability of CdS to its full potential efforts should be directed towards exploring research perspectives such as (1) Improving the nanostructure of developed catalysts to increase active catalytic surface area, resulting in increased synergistic effects. (2) Developing hybrids with the metallic components sites enhanced electrical properties of electro catalysts which correspond to lower overpotential for water-splitting. (3) Charge transfer properties inside electro-catalysts are an area that has not been well investigated.

To conclude, well-defined CdS-NRs@PBNPs heterostructures have been effectively sproduced by employing the solvothermal and ultrasonication methods. Optimized catalyst CdS-NRs@PBNPs(1:1) exhibited exceptional performance and durability in alkaline environment for both HER and OER. The effective movement of electrons in such a hybrid is due to a unique synergistic effect. The improved electrocatalyst had a high HER and OER activity with a low overpotential of 126 mV and 250 mV, respectively, at a current density of 10 $mA.cm^{-2}$. The increased HER and OER activity of hybrid CdS-NRs@PBNPs (1:1), compared to other hybrids, is attributable to the large available active sites that facilitate charge and electron. The catalyst may be suitable for practical usage due to its excellent stability and durability.

5.2. Future Recommendations

Despite the immense developments and many successes, there is still a long way to go before the water splitting process can be integrated for sustainable hydrogen production on commercial scale. To make water-splitting process environmentally and economically competent; future efforts for catalyst design should address certain key prospects such as (i) There is still lack of atomic level in-depth mechanistic investigation of the catalysts. In-depth investigation of the catalysis mechanism offers

realistic direction for optimization of the materials' capability. By employing theoretical simulation and in-situ characterization techniques, kinetics and catalytic mechanism of the process can be effectively studied. (ii) It is impractical to compare the capability of various catalysts due to different procedures being employed for the calculations e.g., different substrate being used for catalysts, different preparation techniques of the electrode, different mass loadings of catalysts, different operating conditions etc. Establishing of standardized testing is really needed to compare different materials obtained studied at different points and time. Objective comparisons of electrocatalyst activity by employing standard methods with identical standard conditions are recommended to effectively convey the results. (iii) Even though a lot of research is being done on the topic of water-splitting. There are still few avenues that needs to be explored in terms of new catalyst material with favorable design structures, characteristics, and active sites. (iv) Charge transfer characteristics of a catalyst are not sufficiently investigated.

References:

[1] Reddy, D.A., et al., Synergetic catalytic behavior of dual metal-organic framework coated hematite photoanode for photoelectrochemical water splitting performance. 2020. **391**: p. 471-479.

[2] Mo, Q., et al., Bimetallic Ni2-xCoxP/N-doped carbon nanofibers: Solid-solution-alloy engineering toward efficient hydrogen evolution. 2019. **244**: p. 620-627.

[3] Nairan, A., et al., NiMo solid solution nanowire array electrodes for highly efficient hydrogen evolution reaction. 2019. **29**(44): p. 1903747.

[4] Ji, X., et al., P-doped Ag nanoparticles embedded in N-doped carbon nanoflake: an efficient electrocatalyst for the hydrogen evolution reaction. 2018. **6**(4): p. 4499-4503.

[5] Guo, C., et al., Approach of fermi level and electron-trap level in cadmium sulfide nanorods via molybdenum doping with enhanced carrier separation for boosted photocatalytic hydrogen production. 2020. **583**: p. 661-671.

[6] Zhao, Y., et al., Layered double hydroxide nanostructured photocatalysts for renewable energy production. 2016. **6**(6): p. 1501974.

[7] Amoretti, M.J.I.J.o.H.E., Towards a peer-to-peer hydrogen economy framework. 2011. **36**(11): p. 6376-6386.

[8] Zahra, R., et al., A review on nickel cobalt sulphide and their hybrids: Earth abundant, pH stable electro-catalyst for hydrogen evolution reaction. 2020.

[9] Rabi, O., et al., An inclusive review on the synthesis of molybdenum carbide and its hybrids as catalyst for electrochemical water splitting. 2020. **494**: p. 111116.

[10] Wang, J., et al., In situ formation of molecular Ni-Fe active sites on heteroatom-doped graphene as a heterogeneous electrocatalyst toward oxygen evolution. 2018. **4**(3): p. eaap7970.

[11] Li, F., et al., Photoluminescence tuning in stretchable PDMS film grafted doped core/multishell quantum dots for anticounterfeiting. 2017. **27**(17): p. 1700051.

[12] Rahman, M.M., M. Alam, and A.M. Asiri, Potential application of mixed metal oxide nanoparticle-embedded glassy carbon electrode as a selective 1, 4-dioxane chemical sensor probe by an electrochemical approach. RSC Advances, 2019. **9**(72): p. 42050-42061.

[13] Sarkar, S., D.J.A.a.m. Basak, and interfaces, Self Powered Highly Enhanced Dual Wavelength ZnO@ CdS Core–Shell Nanorod Arrays Photodetector: An Intelligent Pair. 2015. **7**(30): p. 16322-16329.

[14] Wei, R.-B., et al., Plasmon-enhanced photoelectrochemical water splitting on gold nanoparticle decorated ZnO/CdS nanotube arrays. 2017. **5**(5): p. 4249-4257.

[15] Wei, R.-B., et al., Dual-cocatalysts decorated rimous CdS spheres advancing highly-efficient visible-light photocatalytic hydrogen production. 2018. **231**: p. 101-107.

[16] Cheng, L., et al., CdS-based photocatalysts. Energy & Environmental Science, 2018. **11**(6): p. 1362-1391.

[17] Tang, Z.-R., et al., One dimensional CdS based materials for artificial photoredox reactions. 2017. **5**(6): p. 2387-2410.

[18] Babar, P., et al., Electrocatalytic performance evaluation of cobalt hydroxide and cobalt oxide thin films for oxygen evolution reaction. 2018. **427**: p. 253-259.

[19] Song, J.-P., et al., Catalytically active and chemically inert CdIn 2 S 4 coating on a CdS photoanode for efficient and stable water splitting. 2017. **9**(19): p. 6296-6301.

[20] Wang, Z., et al., Amorphous TiO2 coated hierarchical WO3 Nanosheet/CdS Nanorod arrays for improved photoelectrochemical performance. 2019. **490**: p. 411-419.

[21] Zhan, F., et al., Ce-doped CdS quantum dot sensitized TiO2 nanorod films with enhanced visible-light photoelectrochemical properties. 2018. **455**: p. 476-483.

[22] Kim, W., et al., Enhanced photoelectrochemical and hydrogen production activity of aligned CdS nanowire with anisotropic transport properties. 2019. **463**: p. 339-347.

[23] Liu, Y., et al., Facet and morphology dependent photocatalytic hydrogen evolution with CdS nanoflowers using a novel mixed solvothermal strategy. 2018. **513**: p. 222-230.

[24] Wang, T., et al., Multidimensional CdS nanowire/CdIn 2 S 4 nanosheet heterostructure for photocatalytic and photoelectrochemical applications. 2017. **10**(8): p. 2699-2711.

[25] Pareek, A., et al., Nanostructure Zn–Cu co-doped CdS chalcogenide electrodes for opto-electric-power and H2 generation. 2017. **42**(1): p. 125-132.

[26] Wang, X., et al., Programmable photo-electrochemical hydrogen evolution based on multi-segmented CdS-Au nanorod arrays. 2014. **26**(21): p. 3506-3512.

[27] Wang, L., et al., Heterogeneous p–n junction CdS/Cu2O nanorod arrays: synthesis and superior visible-light-driven photoelectrochemical performance for hydrogen evolution. 2018. **10**(14): p. 11652-11662.

[28] Meng, X.-B., et al., Metal-organic framework as nanoreactors to co-incorporate carbon nanodots and CdS quantum dots into the pores for improved H2 evolution without noble-metal cocatalyst. 2019. **244**: p. 340-346.

[29] Li, N., et al., Noble-metal-free MOF derived hollow CdS/TiO2 decorated with NiS cocatalyst for efficient photocatalytic hydrogen evolution. 2019. **476**: p. 378-386.

[30] Abdullah, U., M. Ali, and E.J.M.C. Pervaiz, An Inclusive Review on Recent Advancements of Cadmium Sulfide Nanostructures and its Hybrids for Photocatalytic and Electrocatalytic Applications. 2021. **508**: p. 111575.

[31] Ali, M., et al., Recent advancements in MOF-based catalysts for applications in electrochemical and photoelectrochemical water splitting: A review. 2021. **45**(2): p. 1190-1226.

[32] Zhou, S., et al., Preparation of heterometallic CoNi-MOFs-modified BiVO4: a steady photoanode for improved performance in photoelectrochemical water splitting. 2020. **266**: p. 118513.

[33] Guan, W., et al., Tailoring magnetic resonance imaging relaxivities in macroporous Prussian blue cubes. 2019. **48**(31): p. 11882-11888.

[34] Guari, Y. and J. Larionova, Prussian Blue-Type Nanoparticles and Nanocomposites: Synthesis, Devices, and Applications: Synthesis, Devices, and Applications. 2019: CRC Press.

[35] Gotoh, A., et al., Simple synthesis of three primary colour nanoparticle inks of Prussian blue and its analogues. 2007. **18**(34): p. 345609.

[36] Wang, J., et al., Recent progress in cobalt-based heterogeneous catalysts for electrochemical water splitting. 2016. **28**(2): p. 215-230.

[37] You, B. and Y.J.A.o.c.r. Sun, Innovative strategies for electrocatalytic water splitting. 2018. **51**(7): p. 1571-1580.

[38] Li, W., C. Wang, and X.J.J.o.M.C.A. Lu, Integrated transition metal and compounds with carbon nanomaterials for electrochemical water splitting. 2021. **9**(7): p. 3786-3827.

[39] Zou, X. and Y.J.C.S.R. Zhang, Noble metal-free hydrogen evolution catalysts for water splitting. 2015. **44**(15): p. 5148-5180.

[40] Morales-Guio, C.G., L.-A. Stern, and X.J.C.S.R. Hu, Nanostructured hydrotreating catalysts for electrochemical hydrogen evolution. 2014. **43**(18): p. 6555-6569.

[41] Lan, Z.-A., G. Zhang, and X.J.A.C.B.E. Wang, A facile synthesis of Br-modified g-C3N4 semiconductors for photoredox water splitting. 2016. **192**: p. 116-125.

[42] Busch, M., et al., Beyond the top of the volcano?–A unified approach to electrocatalytic oxygen reduction and oxygen evolution. 2016. **29**: p. 126-135.

[43] Suen, N.-T., et al., Electrocatalysis for the oxygen evolution reaction: recent development and future perspectives. 2017. **46**(2): p. 337-365.

[44] Wang, X., et al., Electronic and structural engineering of carbon-based metal-free electrocatalysts for water splitting. 2019. **31**(13): p. 1803625.

[45] Vishwakarma, A.K., et al., Band gap engineering of Gd and Co doped BiFeO3 and their application in hydrogen production through photoelectrochemical route. 2017. **42**(36): p. 22677-22686.

[46] Lin, H.-W., et al., Bi-metallic MOFs possessing hierarchical synergistic effects as high performance electrocatalysts for overall water splitting at high current densities. 2019. **258**: p. 118023.

[47] Amano, F., E. Ishinaga, and A.J.T.J.o.P.C.C. Yamakata, Effect of particle size on the photocatalytic activity of WO3 particles for water oxidation. 2013. **117**(44): p. 22584-22590.

[48] Almquist, C.B. and P.J.J.o.C. Biswas, Role of synthesis method and particle size of nanostructured TiO2 on its photoactivity. 2002. **212**(2): p. 145-156.

[49] Anantharaj, S. and V.J.A.E.M. Aravindan, Developments and Perspectives in 3d Transition-Metal-Based Electrocatalysts for Neutral and Near-Neutral Water Electrolysis. 2020. **10**(1): p. 1902666.

[50] Kear, G., F.C.J.C. Walsh, and materials, The characteristics of a true Tafel slope. 2005. **30**(6): p. 51-55.

[51] Lu, J., S. Yin, and P.K.J.E.E.R. Shen, Carbon-encapsulated electrocatalysts for the hydrogen evolution reaction. 2019. **2**(1): p. 105-127.

[52] Anantharaj, S., et al., Recent trends and perspectives in electrochemical water splitting with an emphasis on sulfide, selenide, and phosphide catalysts of Fe, Co, and Ni: a review. 2016. **6**(12): p. 8069-8097.

[53] Wang, J., et al., Earth-abundant transition-metal-based bifunctional catalysts for overall electrochemical water splitting: A review. 2020. **819**: p. 153346.

[54] Liu, K., et al., Recent advances in metal–nitrogen–carbon catalysts for electrochemical water splitting. 2017. **1**(11): p. 2155-2173.

[55] Anantharaj, S., et al., Precision and correctness in the evaluation of electrocatalytic water splitting: revisiting activity parameters with a critical assessment. 2018. **11**(4): p. 744-771.

[56] Shi, Y. and B.J.C.S.R. Zhang, Recent advances in transition metal phosphide nanomaterials: synthesis and applications in hydrogen evolution reaction. 2016. **45**(6): p. 1529-1541.

[57] Tee, S.Y., et al., Recent progress in energy-driven water splitting. Advanced science, 2017. **4**(5): p. 1600337.

[58] Yuan, Y.-J., et al., Cadmium sulfide-based nanomaterials for photocatalytic hydrogen production. Journal of Materials Chemistry A, 2018. **6**(25): p. 11606-11630.

[59] Xie, Y.-M., et al., Ultrathin cadmium sulfide nanosheets for visible-light photocatalytic hydrogen production. 2020. **8**(7): p. 3586-3589.

[60] Jin, Z., et al., Self-assembly of zinc cadmium sulfide nanorods into nanoflowers with enhanced photocatalytic hydrogen production activity. 2020. **567**: p. 357-368.

[61] Zhang, H., et al., Photochemical preparation of atomically dispersed nickel on cadmium sulfide for superior photocatalytic hydrogen evolution. 2020. **261**: p. 118233.

[62] Honda, Y., et al., Photo-Biohydrogen Production by Photosensitization with Biologically Precipitated Cadmium Sulfide in Hydrogen-Forming Recombinant Escherichia coli. 2020. **21**(23): p. 3389-3397.

[63] Gai, Q., et al., Controllable photodeposition of nickel phosphide cocatalysts on cadmium sulfide nanosheets for enhanced photocatalytic hydrogen evolution performance. 2020. **44**(11): p. 4332-4339.

[64] Zhao, W., et al., Facile preparation of Z-scheme CdSAgTiO2 composite for the improved photocatalytic hydrogen generation activity. 2018. **43**(39): p. 18232-18241.

[65] Ai, Z., et al., Band-matching transformation between CdS and BCNNTs with tunable pn homojunction for enhanced photocatalytic pure water splitting. 2020. **69**: p. 104408.

[66] Mani, A.D. and C.J.M.R.B. Subrahmanyam, One pot synthesis of CdS/TiO2 hetero-nanostructures for enhanced H2 production from water and removal of pollutants from aqueous streams. 2016. **73**: p. 377-384.

[67] Liu, L., et al., A transparent CdS@ TiO 2 nanotextile photoanode with boosted photoelectrocatalytic efficiency and stability. 2017. **9**(40): p. 15650-15657.

[68] Jiang, Z., et al., Carbon nitride coupled with CdS-TiO2 nanodots as 2D/0D ternary composite with enhanced photocatalytic H2 evolution: a novel efficient three-level electron transfer process. 2017. **210**: p. 194-204.

[69] Ai, Z., et al., Effective orientation control of photogenerated carrier separation via rational design of a Ti3C2 (TiO2)@ CdS/MoS2 photocatalytic system. 2019. **242**: p. 202-208.

[70] Zhao, H., et al., Blue-edge slow photons promoting visible-light hydrogen production on gradient ternary 3DOM TiO2-Au-CdS photonic crystals. 2018. **47**: p. 266-274.

[71] Wu, K., et al., Synthesis of hollow core-shell CdS@ TiO2/Ni2P photocatalyst for enhancing hydrogen evolution and degradation of MB. 2019. **360**: p. 221-230.

[72] Shinde, P.S., et al., Fabrication of efficient CdS nanoflowers-decorated TiO2 nanotubes array heterojunction photoanode by a novel synthetic approach for solar hydrogen production. 2016. **41**(46): p. 21078-21087.

[73] Huang, L., et al., Two dimensional Ni 2 P/CdS photocatalyst for boosting hydrogen production under visible light irradiation. 2021. **11**(20): p. 12153-12161.

[74] Yang, S., et al., CdS@ Ni3S2 for efficient and stable photo-assisted electrochemical (P-EC) overall water splitting. 2021. **405**: p. 126231.

[75] Manchala, S., et al., High potential and robust ternary LaFeO3/CdS/carbon quantum dots nanocomposite for photocatalytic H2 evolution under sunlight illumination. 2021. **583**: p. 255-266.

[76] Li, Y.-B., et al., Cascade charge transfer mediated by in situ interface modulation toward solar hydrogen production. 2019. **7**(15): p. 8938-8951.

[77] Wang, S., et al., Direct Z-scheme ZnO/CdS hierarchical photocatalyst for enhanced photocatalytic H2-production activity. 2019. **243**: p. 19-26.

[78] Lv, J.-X., et al., In situ synthesis of CdS/graphdiyne heterojunction for enhanced photocatalytic activity of hydrogen production. 2018. **11**(3): p. 2655-2661.

[79] Ning, X., et al., Inhibition of photocorrosion of CdS via assembling with thin film TiO2 and removing formed oxygen by artificial gill for visible light overall water splitting. 2017. **212**: p. 129-139.

[80] Wang, Y., et al., Novel metal doped carbon quantum dots/CdS composites for efficient photocatalytic hydrogen evolution. 2019. **11**(4): p. 1618-1625.

[81] Huang, X., et al., Insight into the piezo-photo coupling effect of PbTiO3/CdS composites for piezo-photocatalytic hydrogen production. 2021. **282**: p. 119586.

[82] Cheng, M., et al., Prussian blue analogue derived magnetic Cu-Fe oxide as a recyclable photo-Fenton catalyst for the efficient removal of sulfamethazine at near neutral pH values. Chemical Engineering Journal, 2019. **362**: p. 865-876.

[83] Liu, Y., et al., Metal sulfide/MOF-based composites as visible-light-driven photocatalysts for enhanced hydrogen production from water splitting. Coordination Chemistry Reviews, 2020. **409**: p. 213220.

[84] Zhou, J.-J., et al., In situ growth of CdS nanoparticles on UiO-66 metal-organic framework octahedrons for enhanced photocatalytic hydrogen production under visible light irradiation. Applied Surface Science, 2015. **346**: p. 278-283.

[85] Xu, H.-Q., et al., Unveiling charge-separation dynamics in CdS/metal–organic framework composites for enhanced photocatalysis. 2018. **8**(12): p. 11615-11621.

[86] Mao, S., et al., Thio linkage between CdS quantum dots and UiO-66-type MOFs as an effective transfer bridge of charge carriers boosting visible-light-driven photocatalytic hydrogen production. 2020. **581**: p. 1-10.

[87] Guo, J., et al., Noble-metal-free CdS/Ni-MOF composites with highly efficient charge separation for photocatalytic H2 evolution. 2020. **522**: p. 146356.

[88] He, J., et al., Significantly enhanced photocatalytic hydrogen evolution under visible light over CdS embedded on metal–organic frameworks. Chemical Communications, 2013. **49**(60): p. 6761-6763.

[89] Wang, Y., et al., Controlled fabrication and enhanced visible-light photocatalytic hydrogen production of Au@ CdS/MIL-101 heterostructure. 2016. **185**: p. 307-314.

[90] Jiang, Z., et al., Assembling Polyoxo-Titanium Clusters and CdS Nanoparticles to a Porous Matrix for Efficient and Tunable H2-Evolution Activities with Visible Light. 2017. **29**(5): p. 1603369.

[91] Shen, L., et al., Noble-metal-free MoS2 co-catalyst decorated UiO-66/CdS hybrids for efficient photocatalytic H2 production. 2015. **166**: p. 445-453.

[92] Bibi, R., et al., Synthesis of Amino-Functionalized Ti-MOF Derived Yolk–Shell and Hollow Heterostructures for Enhanced Photocatalytic Hydrogen Production under Visible Light. 2018. **7**(5): p. 4868-4877.

[93] Reddy, D.A., et al., Designing CdS Mesoporous Networks on Co-C@ Co9S8 Double-Shelled Nanocages as Redox-Mediator-Free Z-Scheme Photocatalyst. 2018. **11**(1): p. 245-253.

[94] Zhang, Y., et al., Well-regulated nickel nanoparticles functional modified ZIF-67 (Co) derived Co3O4/CdS pn heterojunction for efficient photocatalytic hydrogen evolution. 2018. **462**: p. 213-225.

[95] Mao, S., et al., Thio linkage between CdS quantum dots and UiO-66-type MOFs as an effective transfer bridge of charge carriers boosting visible-light-driven photocatalytic hydrogen production. 2021. **581**: p. 1-10.

[96] Jiao, Y., et al., Design of electrocatalysts for oxygen-and hydrogen-involving energy conversion reactions. 2015. **44**(8): p. 2060-2086.

[97] You, B. and Y.J.C. Sun, Chalcogenide and phosphide solid-state electrocatalysts for hydrogen generation. 2016. **81**(10): p. 1045.

[98] Gong, M. and H.J.N.R. Dai, A mini review of NiFe-based materials as highly active oxygen evolution reaction electrocatalysts. 2015. **8**(1): p. 23-39.

[99] Si, F., et al., Bifunctional CdS@ Co 9 S 8/Ni 3 S 2 catalyst for efficient electrocatalytic and photo-assisted electrocatalytic overall water splitting. 2020. **8**(6): p. 3083-3096.

[100] Qu, S., et al., Ni3S2 nanosheet flowers decorated with CdS quantum dots as a highly active electrocatalysis electrode for synergistic water splitting. 2017. **9**(35): p. 29660-29668.

[101] Sheng, W., et al., Phase controlled synthesis and the phase dependent photo-and electrocatalysis of CdS@ CoMo2S4/MoS2 catalyst for HER. 2019. **44**(36): p. 19890-19899.

[102] Garg, P., et al., Computational Screening of Electrocatalytic Activity of Transition Metal-Doped CdS Nanotubes for Water Splitting. 2019. **123**(22): p. 13419-13427.

[103] Wei, L., J. Zhang, and M.J.A.S.S. Ruan, Combined CdS/In2S3 heterostructures with cocatalyst for boosting carriers separation and photoelectrochemical water splitting. 2021. **541**: p. 148431.

[104] Yu, X., et al., Photoelectrochemical water splitting using TiO 2 nanorod arrays coated with Zn-doped CdS. 2021: p. 1-12.

[105] Barrelet, C.J., et al., Synthesis of CdS and ZnS nanowires using single-source molecular precursors. 2003. **125**(38): p. 11498-11499.

[106] !!! INVALID CITATION !!! {}.

[107] Khan, Z.R., M. Zulfequar, and M.S.J.J.o.m.s. Khan, Chemical synthesis of CdS nanoparticles and their optical and dielectric studies. 2011. **46**(16): p. 5412-5416.

[108] Kalasad, M., et al., Temporal evolution of capped cadmium sulfide nanoparticles. 2008. **23**(4): p. 045009.

[109] Barman, J., J. Borah, and K.J.O.A.M. Sarma, Synthesis and characterization of CdS nanoparticles by chemical growth technique. 2008. **2**(12): p. 770-774.

[110] Fu, J., et al., Novel C 3 N 4–CdS composite photocatalysts with organic–inorganic heterojunctions: in situ synthesis, exceptional activity, high stability and photocatalytic mechanism. 2013. **1**(9): p. 3083-3090.

[111] Vidal, J.-C., et al., Amperometric cholesterol biosensors based on the electropolymerization of pyrrole and the electrocatalytic effect of Prussian-Blue layers helped with self-assembled monolayers. 2004. **64**(3): p. 655-664.

[112] Zakaria, M.B., et al., Prussian Blue Derived Nanoporous Iron Oxides as Anticancer Drug Carriers for Magnetic-Guided Chemotherapy. 2015. **10**(7): p. 1457-1462.

[113] Hu, M., et al., Synthesis of Prussian blue nanoparticles with a hollow interior by controlled chemical etching. 2012. **51**(4): p. 984-988.

[114] Yang, J., et al., Green route to Prussian blue nanoparticles with high degradation efficiency of RhB under visible light. 2021. **56**(4): p. 3268-3279.

[115] Hu, H., et al., Yolk-shell Prussian blue nanoparticles with fast ion diffusion for sodium-ion battery. 2019. **249**: p. 206-209.

[116] Kim, H., et al., Rapid removal of radioactive cesium by polyacrylonitrile nanofibers containing Prussian blue. 2018. **347**: p. 106-113.

[117] Khan, R., et al., 3D hierarchical heterostructured LSTN@ NiMn-layered double hydroxide as a bifunctional water splitting electrocatalyst for hydrogen production. 2021. **285**: p. 119174.

[118] Qiang, R., et al., Electromagnetic functionalized Co/C composites by in situ pyrolysis of metal-organic frameworks (ZIF-67). 2016. **681**: p. 384-393.

[119] Xia, X., et al., Highly efficient electrocatalytic hydrogen evolution over edge-modified phosphorene quantum dot/prussian blue skeleton structure. 2019. **374**: p. 401-408.

[120] Zhou, X., et al., Core–Shell-Structured Prussian Blue Analogues Ternary Metal Phosphides as Efficient Bifunctional Electrocatalysts for OER and HER. 2021. **60**(15): p. 11661-11671.

[121] Ma, X., et al., Synthesis of Co-based Prussian Blue Analogues/Dual-Doped Hollow Carbon Microsphere Hybrids as High-Performance Bifunctional Electrocatalysts for Oxygen Evolution and Overall Water Splitting. 2020. **8**(22): p. 8318-8326.

[122] Shen, C.-C., et al., Large improvement of visible-light photocatalytic H 2-evolution based on cocatalyst-free Zn 0.5 Cd 0.5 S synthesized through a two-step process. 2017. **7**(4): p. 961-967.

[123] Li, Z., et al., Mn-Cd-S@ amorphous-Ni3S2 hybrid catalyst with enhanced photocatalytic property for hydrogen production and electrocatalytic OER. 2019. **491**: p. 799-806.

[124] Xiang, R., et al., Self-standing FeCo Prussian blue analogue derived FeCo/C and FeCoP/C nanosheet arrays for cost-effective electrocatalytic water splitting. 2019. **302**: p. 45-55.

[125] Cui, S., Y. He, and X.J.J.o.E.C. Bo, Prussian blue/ZIF-67-derived carbon layers-encapsulated FeCo nanoparticles for hydrogen and oxygen evolution reaction. 2019. **853**: p. 113557.

[126] Pan, Y., et al., Core–shell ZIF-8@ ZIF-67-derived CoP nanoparticle-embedded N-doped carbon nanotube hollow polyhedron for efficient overall water splitting. 2018. **140**(7): p. 2610-2618.